JOURNAL OF GEOPHYSICAL RESEARCH, VOL. 114, C05002, doi:10.1029/2008JC004958, 2009

Indian Ocean intraseasonal sea surface temperature variability during boreal summer: Madden-Julian Oscillation versus submonthly forcing and processes

Benét Duncan[1] and Weiqing Han[1]

Received 12 June 2008; revised 27 December 2008; accepted 2 February 2009; published 5 May 2009.

[1] Intraseasonal sea surface temperature (SST) variability in the Indian Ocean during boreal summer is investigated with a series of experiments using the Hybrid Coordinate Ocean Model (HYCOM). QuickSCAT winds and satellite-observed outgoing longwave radiation (OLR) are used to identify the wind and convection patterns associated with atmospheric intraseasonal oscillations (ISOs). Effects of the Madden-Julian Oscillation (MJO; 30–90 days) and submonthly ISOs are separately examined. Similar to winter, MJO forcing dominates summertime SST variability, even though submonthly forcing is stronger. Wind plays a much larger role in altering SSTs than either shortwave fluxes or precipitation. Different from winter cases, the maximum summertime SST variability shifts to the Arabian Sea (AS) and the Bay of Bengal (BOB), when ISOs also shift to the Northern Hemisphere. In the BOB, surface heat fluxes due to changes in wind speed have a stronger influence on SST than upwelling and advection induced by wind stress, whereas in winter, the effects of surface heat fluxes and oceanic upwelling and advection are comparable. This difference arises from the barrier layer and thin surface mixed layer in the BOB, which reduce the effects of upwelling and amplify the effects of surface heat fluxes. In the AS, surface heat fluxes and entrainment cooling due to changes in wind speed have a larger effect on MJO-scale SST than upwelling induced by wind stress, while the two have comparable effects on submonthly SST. In the equatorial region, wind speed and stress are equally important.

Citation: Duncan, B., and W. Han (2009), Indian Ocean intraseasonal sea surface temperature variability during boreal summer: Madden-Julian Oscillation versus submonthly forcing and processes, *J. Geophys. Res.*, *114*, C05002, doi:10.1029/2008JC004958.

1. Introduction

1.1. Atmospheric Intraseasonal Oscillations

[2] Indian Ocean (IO) intraseasonal oscillations (ISOs) range in scale from 10 to 90 days. On 30–90 day time scales, the Madden-Julian Oscillation (MJO) [e.g., *Madden and Julian*, 1971, 1972] dominates ISOs. On 10–30 day submonthly time scales, convectively coupled Kelvin and Rossby waves dominate the ISOs [*Kiladis and Weickmann*, 1997; *Wheeler and Kiladis*, 1999; *Chatterjee and Goswami*, 2004, and references therein]. Their important component, the Quasi-Biweekly Mode (QBM), is thought to be a Rossby wave that is shifted northward (southward) by the mean flow during summer (winter) [*Murakami and Frydrych*, 1974; *Chen and Chen*, 1993; *Numaguti*, 1995; *Chatterjee and Goswami*, 2004]. Observations from the Bay of Bengal Monsoon Experiment (BOBMEX) show that submonthly convection and winds are much stronger than those of the MJO [*Bhat et al.*, 2001; see also *Vincent et al.*, 1998]. MJOs travel both eastward and northward during boreal summer with global zonal wave numbers 1–3 [*Li and Wang*, 1994; *Hendon and Salby*, 1996; *Kiladis and Weickmann*, 1997; *Wang and Xie*, 1997; *Webster et al.*, 2002], whereas the QBM propagates westward with zonal wave numbers 5–6 [*Kiladis and Weickmann*, 1997].

[3] It is suggested that submonthly ISOs together with the MJO can determine the amplitude and phase of the wet and dry spells of the Asian summer monsoon and the Australian monsoon [*Sikka and Gadgil*, 1980; *Yasunari*, 1981; *Krishnamurti and Subramanyam*, 1982; *Webster*, 1983; *Lau and Chan*, 1985; *McBride*, 1987; *Krishnamurti et al.*, 1988; *Wang and Xie*, 1997; *Webster and Hoyos*, 2004; *Lau and Waliser*, 2005, and references therein]. Recent studies have also shown that many ISOs generated in the IO can propagate to the Pacific and impact the El Nino Southern Oscillation (ENSO) [*McPhaden*, 1999; *Moore and Kleeman*, 1999; *Takayabu et al.*, 1999; *Kessler and Kleeman*, 2000; G. Kiladis and K. Straub, Forcing of the equatorial ocean by an atmospheric Kelvin wave, paper presented at the 13th Conference on Atmospheric and Oceanic Fluid Dynamics, American Meteorological Society, Breckenridge, Colorado, 2001], and can affect the onset and termination of the IO dipole (IOD) [*Saji et al.*, 1999; *Webster et al.*, 1999; *Murtugudde et al.*, 2000; *Yu and Rienecker*, 2000; *Rao and Yamagata*, 2004; *Han et al.*, 2006a]. Importantly, air-sea

[1]Department of Atmospheric and Oceanic Sciences, University of Colorado, Boulder, Colorado, USA.

0148-0227/09/2008JC004958$09.00

interactions over the IO can have a significant influence on ISO propagation [*Flatau et al.*, 1997; *Wang and Xie*, 1998; *Waliser et al.*, 1999; *Kemball-Cook and Wang*, 2001; *Woolnough et al.*, 2001; *Fu et al.*, 2003; *Inness and Slingo*, 2003; *Sperber et al.*, 2005]. Realistic simulation of ISOs in climate models, however, is still a challenge [*Slingo et al.*, 1996; *Sperber et al.*, 2005; *Lin et al.*, 2006], which underlines the need for further knowledge about coupled processes. To this end, investigating intraseasonal sea surface temperature (SST) variability is key to an increased understanding of coupled processes on intraseasonal time scales.

[4] A large number of studies on IO intraseasonal SST variability exist [e.g., *McPhaden*, 1982; *Krishnamurti et al.*, 1988; *Hendon and Glick*, 1997; *Jones et al.*, 1998; *Shinoda and Hendon*, 1998; *Shinoda et al.*, 1998; *Woolnough et al.*, 2000; *Harrison and Vecchi*, 2001; *Sengupta et al.*, 2001; *Schiller and Godfrey*, 2003; *Waliser et al.*, 2003, 2004; *Duvel et al.*, 2004; *Kessler*, 2005; *Han et al.*, 2006b; *Saji et al.*, 2006; *Han et al.*, 2007]. These studies show divergent views of the processes that determine intraseasonal SST variability, and the relative importance of MJO and submonthly ISOs is not addressed for boreal summer. *Han et al.* [2007] summarized detailed aspects of the studies, and first investigated IO SST variability on both MJO and submonthly time scales for the winter monsoon. For comparison, here we provide a comprehensive study of SST variability during the summer monsoon.

1.2. Present Research

[5] This paper will provide a detailed investigation of the impacts of the MJO and submonthly ISOs on SST during boreal summer. To ensure consistency for comparison with *Han et al.* [2007], we analyze the same set of experiments using the Hybrid Coordinate Ocean Model (HYCOM) to evaluate the importance of oceanic dynamical processes, mixed layer physics, and surface heat fluxes. Section 2 details our data, model, and experiment design. In section 3, we discuss our results, while section 4 provides a summary and discussion.

2. Data and Model

2.1. Data

[6] Observed SST, outgoing longwave radiation (OLR), and winds are used to validate HYCOM solutions and to identify ISOs. Our period of interest is 1998–2004, when all the following data sets are available. Satellite observed daily OLR from the National Oceanic and Atmospheric Administration (NOAA) [*Liebmann and Smith*, 1996] and 3-day mean winds from QuickSCAT [*Tang and Liu*, 1996] are used to document ISOs. Prior to July 1999, when QuickSCAT winds do not exist, 3-day ECMWF reanalysis (ERA-40) winds are used. The 3-day mean Tropical Rainfall Measuring Mission (TRMM) SST with $0.25^\circ \times 0.25^\circ$ resolution is analyzed and compared with the model solution. To remove missing values, the TRMM SST is first averaged onto $2.5^\circ \times 2.5^\circ$ grids, and the few missing values left are then filled by linear spatial and temporal interpolation [*Han et al.*, 2007].

[7] Additionally, shortwave (SW) radiation and wind data during 21 October 2001–4 June 2004 from Triangle Trans-Ocean Buoy Network (TRITON) floats at 90°E, 1.5°S is analyzed. Two periods of continuous TRITON wind data are available for our range of years, from 23 October 2001 to 27 August 2002, and from 12 July 2003 to 8 June 2004. Vertical temperature and salinity profiles from Argo floats in the Bay of Bengal (BOB) are also studied. Monthly climatologies of temperature and salinity from the World Ocean Atlas 2005 (WOA05) are used to derive mixed layer thickness. Note that near Sumatra and the BOB coasts, WOA05 has very few data points and thus the estimated mixed layer depths may not be reliable in these regions.

2.2. Hybrid Coordinate Ocean Model Configuration and Validation of Forcing Fields

[8] HYCOM utilizes terrain-following coordinates in coastal regions, isopycnal coordinates in the interior open ocean, and z coordinates in weakly stratified and surface layers, and in very shallow waters [e.g., *Bleck*, 2002; *Halliwell*, 2004]. In the present experiments, the K-profile parameterization [*Large et al.*, 1994, 1997; *Large and Gent*, 1999] is chosen as the vertical mixing scheme. HYCOM has been applied in studies of interannual and intraseasonal variability and the seasonal cycle in the Indian and Atlantic Oceans [*Han et al.*, 2004; *Han*, 2005; *Han et al.*, 2006a, 2006b; *Yuan and Han*, 2006; *Han et al.*, 2007]. Since the HYCOM configuration and experiment design are explained in detail in *Han et al.* [2007], we only provide a brief discussion here.

[9] HYCOM is configured to the IO basin north of 30°S with 18 vertical layers and a horizontal resolution of $0.5^\circ \times 0.5^\circ$. To better resolve the mixed layer, thermocline, and barrier layer, the vertical layers have a fine resolution in the upper ocean. For example, the mean interface depths of the upper 10 layers, averaged over the BOB from 1999 to 2003, are approximately 3, 48, 138, 151, 161, 169, 178, 191, 208, and 234 m. SW radiation penetration is parameterized with Jerlov water type IA [*Jerlov*, 1976]. No-slip conditions are applied along continental boundaries. Near the southern boundary (25°–30°S), a 5°-wide sponge layer is applied to relax model temperature and salinity fields to *Levitus and Boyer* [1994] and to *Levitus et al.* [1994] climatology. Lateral boundary forcing due to the Indonesian Throughflow and BOB rivers is included by relaxing model temperature and salinity to Levitus data in the corresponding regions.

[10] Primary forcings used are 3-day QuickSCAT winds, International Satellite Cloud Climatology Project Flux Data (ISCCP-FD) SW and longwave radiative fluxes [*Zhang et al.*, 2004], Climate Prediction Center Merged Analysis of Precipitation (CMAP) pentad data [*Xie and Arkin*, 1996], and ERA-40 and National Centers for Environmental Prediction (NCEP) air temperature and specific humidity for 1998–2004 (see *Han et al.* [2007] for details). Wind stress (τ) is calculated using QuickSCAT wind speed ($|\mathbf{V}|$) in a standard bulk formula $\tau = \rho_a C_D |\boldsymbol{V}| \boldsymbol{V}$. Here, ρ_a is the density of air (1.175 kg/m^3), C_D is a drag coefficient (0.0015), and $\mathbf{V}$ is the QuickSCAT wind vector. Surface latent and sensible heat fluxes are then calculated using winds, air temperature, specific humidity, and HYCOM SST in the flux parameterizations of *Kara et al.* [2000].

[11] Validity of these forcing fields was discussed by *Han et al.* [2007]. Here, we provide further validation. Figure 1 shows the variance spectra of zonal and meridional wind

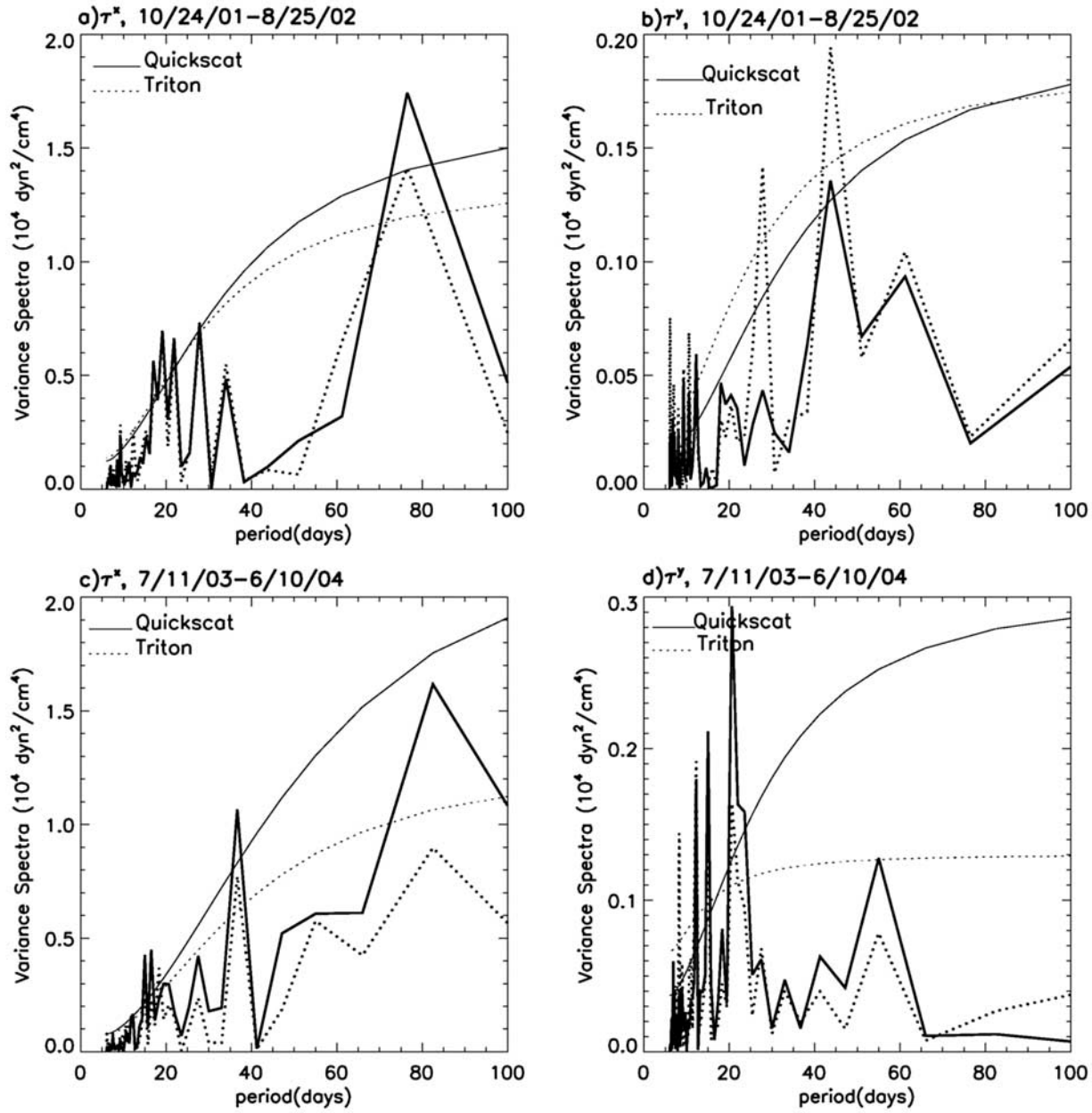

Figure 1. (a) Variance spectra of zonal wind stress τ^x, from QuickSCAT (bold line) and TRITON (bold dashed line) observations for 24 October 2001 to 25 August 2002 at 90°E, 1.5°S. The thin solid/dashed lines show the 90% significance level for each. (b) Same as Figure 1a but for meridional wind stress τ^y. (c) Same as Figure 1a but for 11 July 2003 to 10 June 2004. (d) Same as Figure 1c but for meridional wind stress. The wind stress for TRITON is calculated using the same formula as that for QuickSCAT. Units are $dyn^2\ cm^{-4}$.

stresses from QuickSCAT and TRITON data at 90°E, 1.5°S. Both the TRITON and QuickSCAT wind stresses contain essentially the same spectral peaks at 10–30 day and 30–90 day periods, albeit with some quantitative differences. Owing to the short duration of the TRITON data records, some spectral peaks do not exceed the 90% confidence level. Quantitative comparison between ERA-40 and QuikSCAT wind stress demonstrates that ERA-40 winds are able to capture the observed intraseasonal variabilities rather well, but their amplitudes tend to be stronger than the QuikSCAT winds. After the ERA-40 wind speed is scaled down to 90%, the amplitudes of the ERA-40 winds agree very well with the QuikSCAT winds. Variance spectra of the scaled ERA-40 and QuickSCAT wind stress are shown in Figure 2 for a period of overlap (1 August 1999–31 December 2001) in the BOB (80–90°E, 4–15°N). Note that the wind stress data is averaged over the BOB before performing the spectral analysis. Both the zonal and meridional wind stresses contain similar peaks over the intraseasonal periods, but the magnitudes of the ERA-40 peaks are greater than those from QuickSCAT at 40–60 days (Figure 2a). The shape of the ERA-40 and QuickSCAT

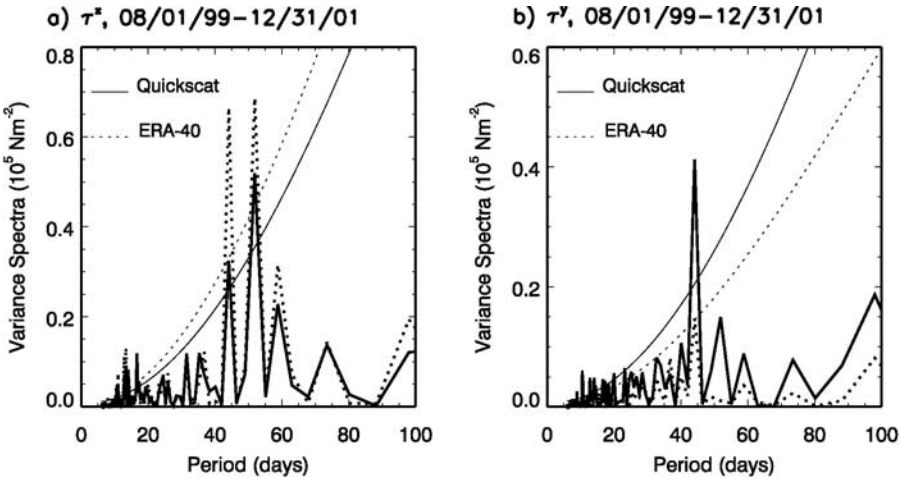

Figure 2. (a) Variance spectra of zonal wind stress τ^x, for QuickSCAT observations (bold line) and scaled ERA-40 reanalysis (bold dashed line) from 1 August 1999 to 31 December 2001, averaged over the western Bay of Bengal (BOB) (80°–90°E, 4°–15°N). The thin solid/dashed lines show the 90% significance level for each. (b) Same as Figure 2a but for meridional wind stress τ^y. Units are newtons per meter squared.

spectra are also very similar over the eastern equatorial IO for the same time period (not shown). On the basis of these comparisons, the scaled ERA-40 winds are used to force HYCOM before July 1999. This specific detail is also true in *Han et al.* [2006a, 2007], although it is not explicitly stated there.

[12] Similarly, intraseasonal variability of net SW radiation from the TRITON observations is reasonably reproduced by the ISCCP data from 21 October 2001 to 4 June 2004 (Figure 3). Note that an albedo of 3% is applied to the TRITON data because it measures the total downward, rather than the net, SW radiation. The correlation coefficient between the two curves is 0.75. The standard deviations (STDs) for ISCCP and TRITON SW radiation are 41.7 W m^{-2} and 48.6 W m^{-2}, respectively, indicating that ISCCP may underestimate the SW flux variability by approximately 14%.

2.3. Experiments

[13] Seven model experiments are performed for the period of 1998–2004. They are listed in Table 1 and

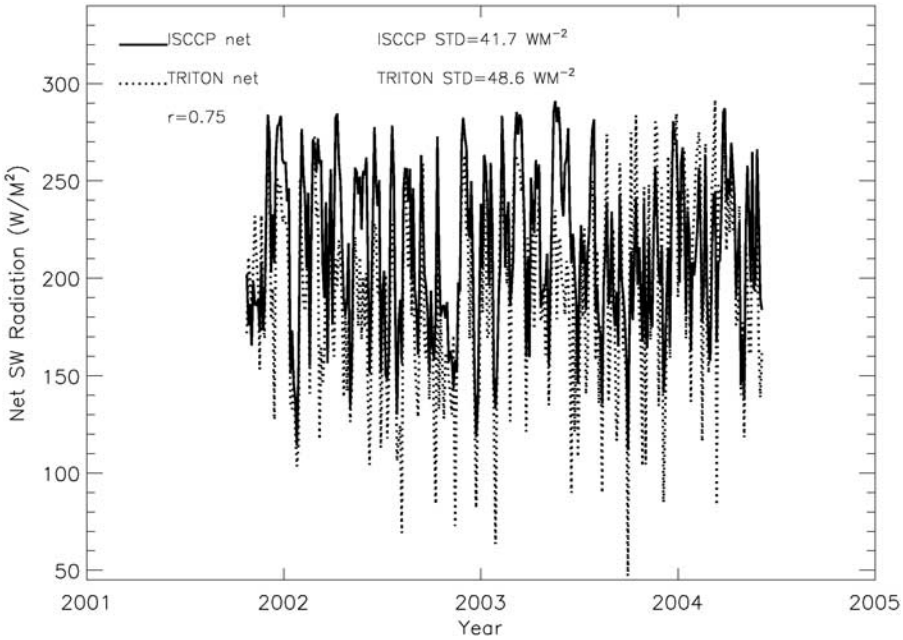

Figure 3. Time series of TRITON (dashed line) and ISCCP (solid line) net SW radiation from 21 October 2001 to 4 June 2004 at 90°E, 1.5°S. Earth's surface albedo of 3% is applied to the TRITON data. Standard deviations (STD) of both ISCCP and TRITON SW radiation are displayed, along with the correlation coefficient (r) between the two. Units are watts per meter squared.

Table 1. Hybrid Coordinate Ocean Model Experiments and Forcings Used[a]

Experiment Number	Forcings Used
MR	All 3-day mean forcing fields: winds, fluxes, precipitation
EXP1	Low-passed (removed less than) 105 days
EXP2	Low-passed (removed less than) 30 days
EXP3	Low-passed wind stress
EXP4	Low-passed wind stress and speed
EXP5	Low-passed shortwave flux
EXP6	Low-passed precipitation

[a]Low-pass frequency is 105 days, unless otherwise noted.

summarized below. See *Han et al.* [2007] for details regarding the model spin-up and other aspects of the experiments.

[14] The main run (MR) is forced by the complete 3-day mean fields discussed in section 2.2. As such, it is the most complete solution, and it is used to evaluate the ocean response due to all forcings. Experiment 1 (EXP1) is forced by low-passed 105-day fields using a Lanczos filter [*Duchon*, 1979]. The low-passed fields remove any signals with periods shorter than 105 days. The difference solution MR – EXP1, then, isolates the ocean response to ISOs. Similarly, EXP2 employs a low-pass 30-day filter to remove any variability shorter than 30 days from the forcing fields. It follows that MR – EXP2 isolates the effects of submonthly variability, while EXP2 – EXP1 estimates the ocean response to 30–90 day ISOs, which are dominated by MJO events. EXP3 is forced by low-passed 105 day wind stress, so it excludes the effects of intraseasonal Ekman convergence and divergence (which can affect upwelling) as well as anomalous advection. EXP4 is forced by low-passed 105-day wind stress and wind speed. It excludes the same effects as EXP3, with the additional exclusion of intraseasonal wind speed, which can affect the SST via latent and sensible heat fluxes and entrainment cooling. This is because the entrainment rate depends on the frictional velocity u^*, which is directly associated with the wind speed $|\mathbf{V}|$ in our experiments because $u^* = \sqrt{(|\tau|\rho_a)} = \sqrt{(c_D|\mathbf{V}|)}$. Therefore, when $|\mathbf{V}|$ is filtered, the entrainment rate is affected. EXP5 is forced by low-passed 105 day SW flux, and EXP6 by low-passed 105 day precipitation, which can impact the SST by changing stratification and the mixed layer thickness (hm). Then, the difference solutions MR – EXP3, MR – EXP4, EXP3 – EXP4, MR – EXP5, and MR – EXP6 isolate the ocean response to intraseasonal wind stress, total winds, wind speed, SW radiation, and precipitation, respectively.

3. Results

3.1. Madden-Julian Oscillation (MJO) and Submonthly Intraseasonal Oscillations (ISOs)

[15] Large values of STD in the OLR fields of Figures 4a–4c indicate where strong variations in convection are located on each time scale. On 10–90 day time scales (Figure 4a), strong changes in convection ($\geq$28W m^{-2}) occur in the central-eastern equatorial ocean, the BOB, and the eastern Arabian Sea (AS), where the mean SST exceeds 28°C (Figure 5). While the convective variability associated with both submonthly ISOs and MJO events has similar spatial patterns, it appears that the former has a larger amplitude than the latter. Associated with the strong changes in convection, QuickSCAT wind speed (Figures 4d–4f) and stress curl (Figures 4g–4i) also show large-amplitude variations in the central-eastern equatorial basin, the BOB, the AS, and the southeast tropical IO. Again, submonthly events show larger amplitude variation than MJO events in most regions except the AS. This is consistent with *Bhat et al.* [2001].

3.2. Validation of the Simulated Intraseasonal Sea Surface Temperature

[16] Over all seasons, the largest intraseasonal SST variability occurs in a region that stretches across the southern tropical IO, western AS, the BOB, and the eastern equatorial ocean (Figures 6a and 6b). The variability south of the equator is a major feature of the winter months that coincides with the location of the winter intertropical convergence zone (ITCZ), which has been investigated in several existing studies [e.g., *Harrison and Vecchi*, 2001; *Duvel et al.*, 2004; *Saji et al.*, 2006; *Han et al.*, 2007].

[17] During summer, the region of large amplitude SST change shifts to the northern IO (Figure 6c), where maxima in convection and winds are located (Figures 4a, 4d, and 4g). Averaged over summer months from 1999 to 2003, HYCOM reasonably simulates many of the major SST features at all time scales (Figures 6c–6h), albeit with some quantitative differences. For example, strong SST variations in the AS, the BOB, and the eastern equatorial ocean are all reasonably simulated. An evident exception is the strong variability south of the equator in HYCOM, which does not occur in TRMM data during the summer season (Figures 6c–6h). As shown by *Han et al.* [2007], this model/data discrepancy is likely because HYCOM has a much thinner mixed layer than is observed in the region, which makes it more sensitive to surface forcing.

[18] To further quantify model/data comparisons, we choose three regions (labeled in Figure 6c) that are identified as having large variability in winds, OLR, and SST (Figures 4 and 6). Region 1 is located in the central AS (55–73°E, 2–14°N), Region 2 is in the western BOB (80–90°E, 4–15°N), and Region 3 is in the eastern equatorial IO warm pool (84°–96°E, 3°S–5°N). Figure 7 provides a time series of intraseasonal SST in each region from 2000 to 2003, as observed by TRMM (thick solid line) and as simulated by HYCOM MR (dashed line) and by HYCOM MR – EXP1 (thin solid line), which represents the SST forced by ISOs only. Model-data correlations for regions 1, 2, and 3 are 0.66, 0.65, and 0.69 respectively, with significance above 95%. Note that the significance test takes into account the reduced degree of freedom due to the filter [*Livezey and Chen*, 1983]. These correlations are lower than those from the ITCZ region used in the wintertime study [*Han et al.*, 2007], but they are similar in magnitude to those from the warm pool and the AS in the same study. Looking at events with magnitudes larger than 1 STD, HYCOM performs reasonably well, although it occasionally over- or underestimates SST changes. MJO-scale events are simulated well by HYCOM, with model-data correlation coefficients of 0.71, 0.70, and 0.76 in regions 1, 2, and 3, respectively (Figure 8a for region 2), while submonthly events

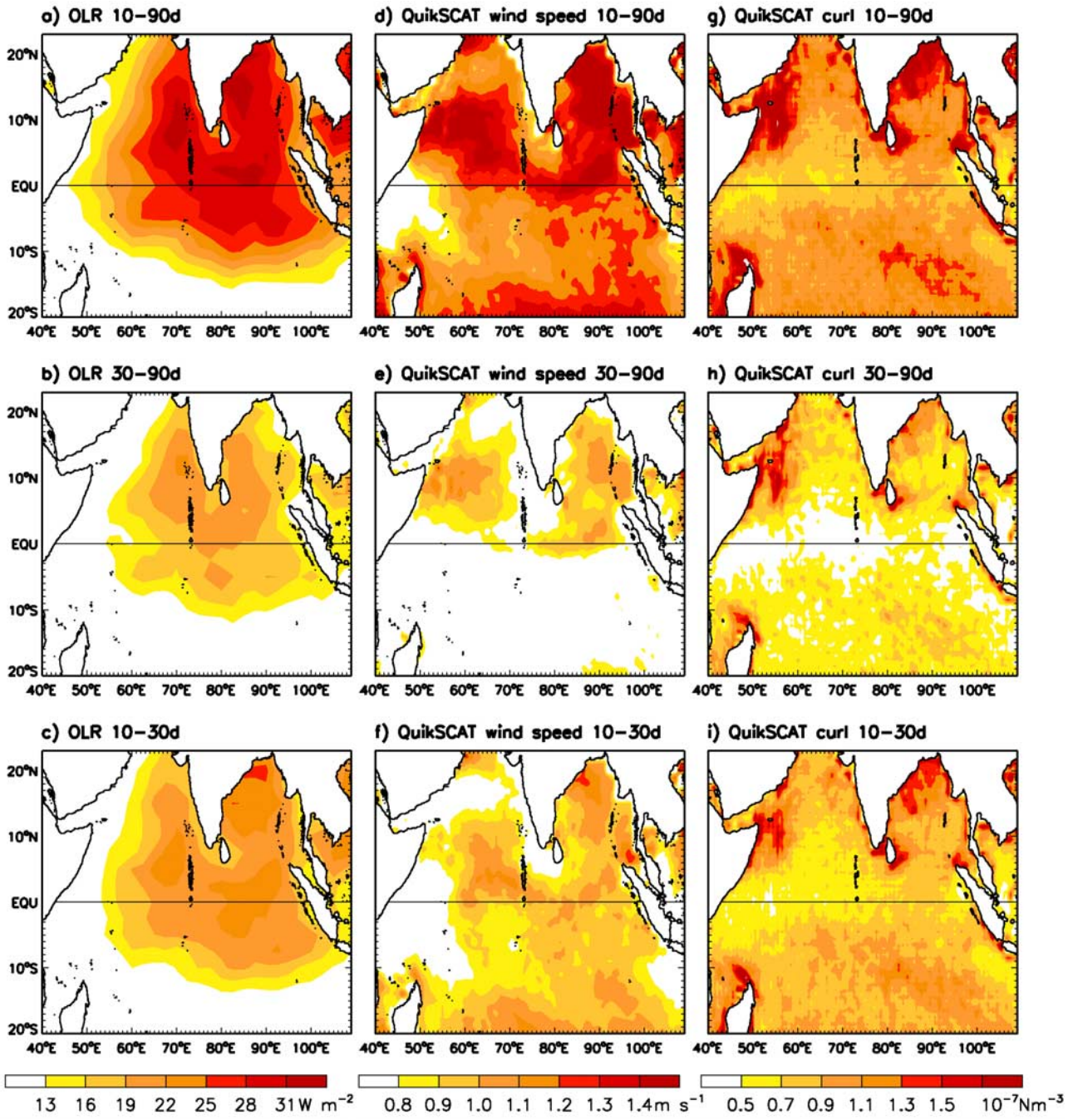

Figure 4. (a) STD of 10–90 day band-pass-filtered outgoing longwave radiation (OLR) over the tropical Indian Ocean (IO) during boreal summer (May–October) from 1999 to 2003. (b) Same as Figure 4a except filtered to 30–90 days. (c) Same as Figure 4a except filtered to 10–30 days. (d) STD of 10–90 day band-pass-filtered QuickSCAT wind speed during boreal summer from 1999 to 2003. ERA-40 winds are used before July 1999. (e) Same as Figure 4d but filtered to 30–90 days. (f) Same as Figure 4d but filtered to 10–30 days. (g) STD of 10–90 day band-passed QuickSCAT wind stress curl during boreal summer from 1999 to 2003. (h) Same as Figure 4g but filtered to 30–90 days. (i) Same as Figure 4g but filtered to 10–30 days. Units are watts per meter squared for OLR, meters per second for wind speed, and 1×10^{-7} newtons per meter cubed for wind stress curl.

have somewhat lower model-data correlations (Figure 8b for region 2).

[19] The variance spectra of summertime TRMM and HYCOM MR SST anomalies from 1999 to 2003 provide an additional look at HYCOM's performance in each of the three regions (Figure 9). To do this, we average the TRMM and HYCOM MR summertime SST time series over each region, and then perform a spectral analysis in which the annual and semiannual cycles are removed. The variance spectra of the two data sets generally agree well in all three

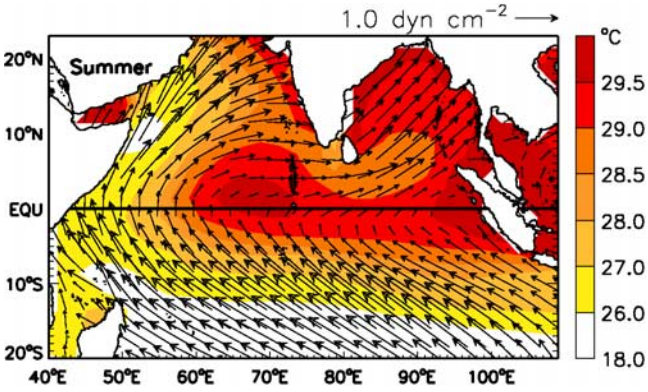

Figure 5. Summertime (May–October) mean sea surface temperature (SST) from the Tropical Rainfall Measuring Mission (TRMM) (shaded contours) for the period 1998–2004 and wind stress from QuickSCAT (arrows) for the period 1998–2003. ERA-40 wind stress was used before July 1999. Units are degrees Celsius for SST and dyn cm^{-2} for wind stress.

regions, with some exceptions. The most notable model/data difference occurs in the BOB (Figure 9b), where a strong 90-day peak appears in the HYCOM solution but not in the TRMM data.

[20] Overall, HYCOM reasonably simulates SST in the three chosen regions. Existing discrepancies may be due to model errors, data errors, uncertainties in the model forcing fields, and differences between TRMM skin temperature and the model bulk temperature. Model-data differences in coastal regions may be due to the artificial interpolation of QuickSCAT winds to land where their values are zero [*Han et al.*, 2007]. Differences may also be due to the model's thick mixed layer and deep thermocline, a topic which is investigated in more detail in section 3.5.1.

[21] Amplitudes of the SST variability shown in Figure 7 are large, with maximum warming (cooling) of 0.83°C (1.09°C) in the eastern equatorial IO warm pool, 0.78°C (1.08°C) in the BOB and 0.67°C (0.73°C) in the AS. Even small SST changes in these regions can have a very important effect on convection because mean summer SSTs there exceed 28–29°C (Figure 5). At such a high SST, small temperature changes can have large impacts on convection [e.g., *Fu et al.*, 1994; *Bajuk and Levoy*, 1998; *Del Genio and Kovari*, 2002].

3.3. Impact of Atmospheric ISOs

[22] Of particular interest is that while winds and OLR variations are larger during submonthly events (Figure 4), amplitudes of summer SST variability are larger during MJO events (Figure 6). This is true even in the BOB, where submonthly ISOs are much stronger than the MJO-scale ISOs. The same is true during winter, as discussed in *Han et al.* [2007]. Following the discussion in *Han* [2005], this skew of frequency between the peak forcing and response is likely because it is the time derivative of SST, rather than the SST itself, that is proportional to the strength of the forcing. Total changes in SST during an event are found by integrating the forcings over the event duration. That is, even though the amplitude of submonthly forcing is larger than that for the MJO, it does not act on the ocean long enough to cause as large an SST change as is induced by the MJO forcing.

[23] Intraseasonal SST changes can also result from oceanic internal variability [*Jochum and Murtugudde*, 2005; *Han et al.*, 2007]. In this study, we focus on understanding air-sea interactions related to ISOs. The high correlation coefficients (0.81–0.98) between 10 and 90 day SSTs from the MR (due to both ISO forcing and internal variability) and the difference solution, MR – EXP1 (mainly due to ISO forcing), demonstrate the dominance of ISO forcing (Figure 7). HYCOM MR and the difference solution can occasionally differ significantly, likely because of internal variability. This is in agreement with *Waliser et al.* [2004], who found that ISO forcing dominates instabilities over the IO.

3.4. Processes: General Analysis

[24] A time series of intraseasonal SST changes caused by SW radiation, precipitation, and wind (via entrainment, turbulent heat fluxes, advection, and upwelling) is calculated for each region over both MJO and submonthly time scales. Owing to the high degree of similarity for all regions, only region 2 (the BOB) is shown in Figure 10. In all regions, SST variability on both MJO and submonthly time scales is dominated by wind (red line of Figures 10a and 10c), while the effects of SW radiation and precipitation (blue and yellow curves) are weak. On 30–90 day time scales, correlation coefficients between the total SST change due to all ISO forcings (black curve in Figure 10a) and due to the total wind (red curve) is 0.95 in the AS, 0.93 in the BOB, and 0.96 in the eastern equatorial IO. On 10–30 day time scales, the correlations are the same as shown above (Figure 10c). The high correlation coefficients demonstrate the deterministic role played by winds in causing summertime intraseasonal SST variability, as during wintertime [*Han et al.*, 2007].

[25] Different from the winter, when the largest SST change occurs in the ITCZ and equatorial regions due almost equally to both oceanic upwelling and advection associated with changes in wind stress (see section 2.3) and turbulent heat fluxes and entrainment cooling associated with changes in wind speed [*Han et al.*, 2007], the strongest summertime variability in the BOB is mostly due to wind speed, with wind stress playing a lesser role (Figures 10b and 10d). Entrainment and turbulent heat fluxes due to changes in wind speed have an apparently larger effect than upwelling and advection on SST variability for almost every MJO and submonthly scale event, albeit to a lesser extent for submonthly ISOs (Figure 10d). The MJO-scale (submonthly) SST correlation coefficient between total wind and wind speed forcing is 0.93 (0.90), while that for wind stress is 0.77 (0.84). The reasons for the importance of wind speed in the BOB will be discussed in section 3.5.1.

[26] In the AS, wind speed also has a larger effect than wind stress on MJO-scale SST variability (Figure 11a), with a correlation coefficient of 0.95 between the SSTs induced by total wind and wind speed, and 0.84 between total wind and stress forcing. On submonthly time scales, SST variability in the AS results almost equally from wind stress and wind speed (Figure 11b). In the warm pool (region 3), wind speed and stress (Figures 11c and 11d) seem to contribute

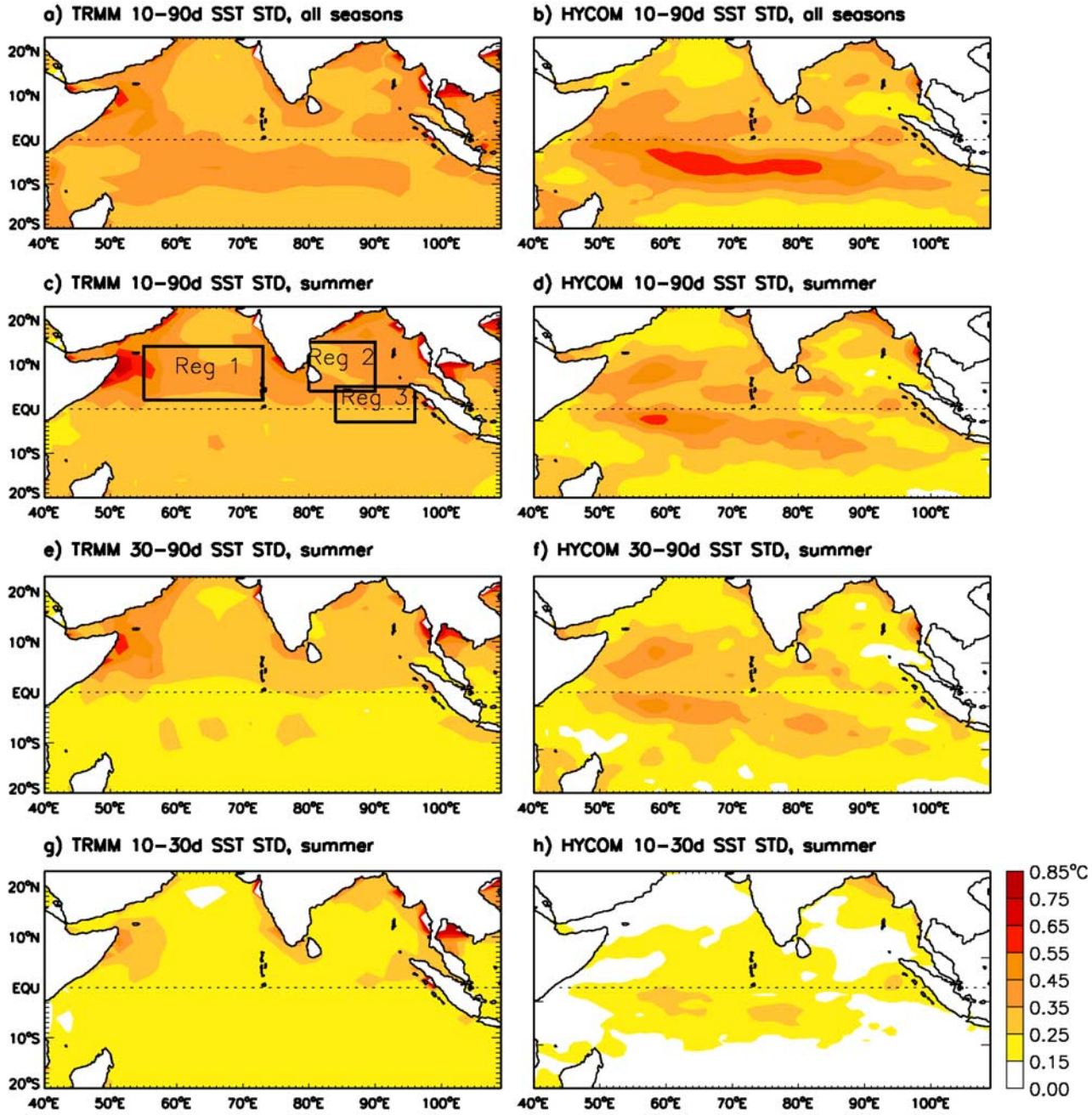

Figure 6. (left) Observed and (right) modeled SST STD, 1999–2003. (a) STDs of 10–90 day filtered TRMM SST based on all months from 1999 to 2003. (b) Same as Figure 6a but for Hybrid Coordinate Ocean Model (HYCOM) main run (MR). (c) Same as Figure 6a but for boreal summer months (May–October) only. Boxed regions represent the Arabian Sea (AS) (region 1), the BOB (region 2), and the eastern equatorial warm pool (region 3) and are discussed in section 3. (d) Same as Figure 6c but for HYCOM MR. (e) Same as Figure 6c but for 30–90 day filtered TRMM SST. (f) Same as Figure 6e but for HYCOM MR. (g) Same as Figure 6c but for 10–30 day filtered TRMM SST. (h) Same as Figure 6g but for HYCOM MR. Units are degrees Celsius.

almost equally on both submonthly and MJO time scales. This is also true in the equatorial region surrounding the Maldives (not shown), where wind forcing is strong on submonthly time scales (Figures 4f and 4i).

[27] In studying specific MJO and submonthly events (see below), it is clear that SW radiation and precipitation can make nonnegligible contributions to overall SST variability in some regions. The ratios STD_{SW}/STD_{all} and STD_{pr}/STD_{all}, which measure the ratio of SST STD forced by total ISOs and by SW radiation and precipitation only, are calculated using STD values for each region and for each time scale. SW forcing has the largest relative ampli-

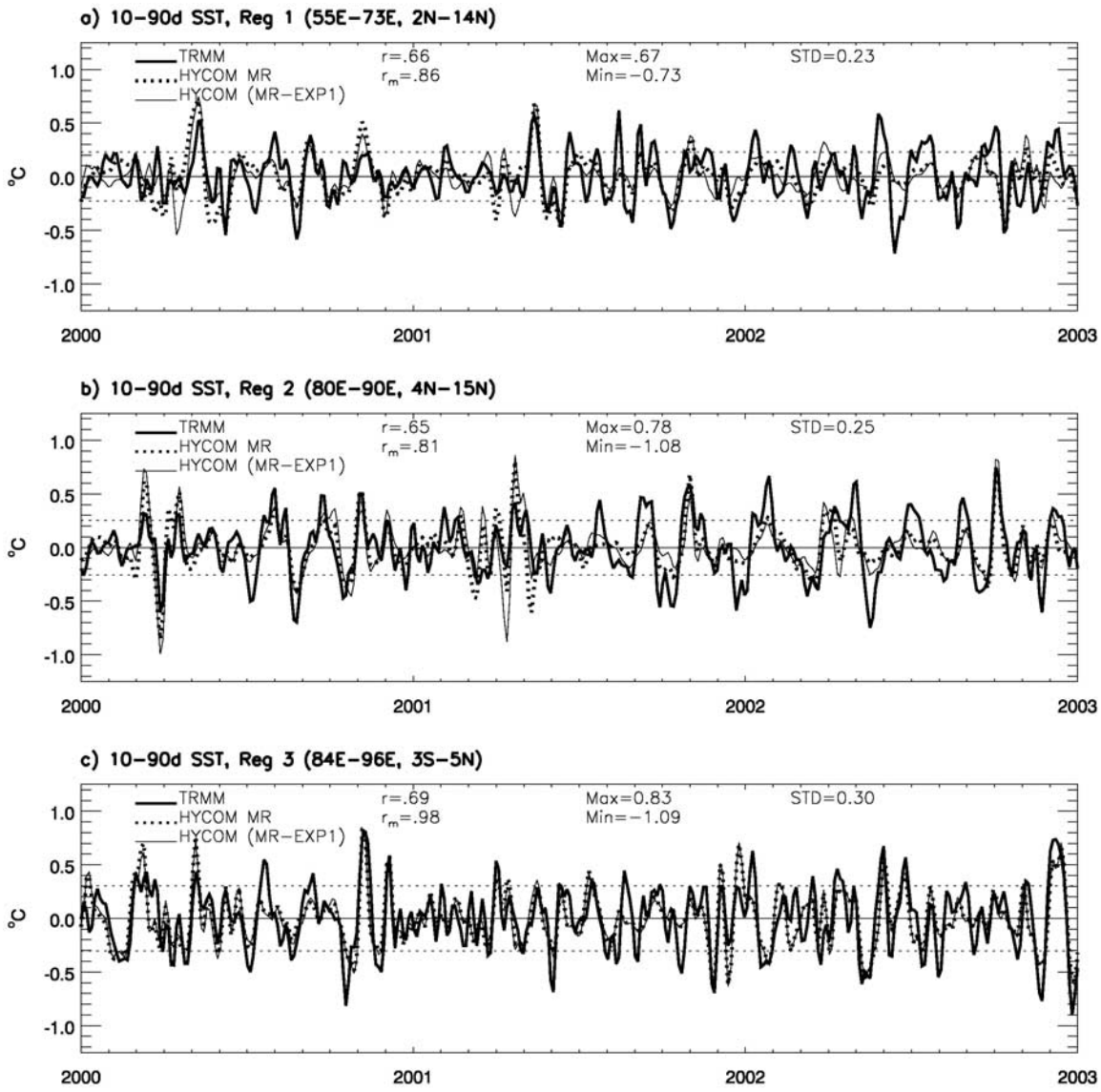

Figure 7. (a) Time series of 10–90 day SST averaged over region 1 (AS) in Figure 6c, from 2000 through 2002. The bold and dashed lines represent the TRMM and HYCOM MR SSTs, respectively. The thin solid line represents the SST from HYCOM difference solution MR – EXP1, which isolates the effect of ISOs only. The horizontal dashed line represents the STD of TRMM SST. Correlation coefficients between SSTs from HYCOM MR and TRMM (r) and HYCOM MR - EXP1 (r_m) are calculated for the years 1999–2003 and displayed. (b) Same as Figure 7a but for the BOB region 2 in Figure 6c. (c) Same as Figure 7a but for the warm pool region 3 in Figure 6c. Units are degrees Celsius.

tude in the warm pool on both MJO (ratio = 0.22) and submonthly (ratio = 0.23) scales. Precipitation has the largest relative amplitude in the BOB for MJO time scales (ratio = 0.125) and in the warm pool for submonthly scales (ratio = 0.154).

[28] The overarching dominance of winds on ISO-induced SST variability is in agreement with winter events [*Han et al.*, 2007] and with *Waliser et al.*'s [2004] study of boreal summer canonical ISOs. The latter study, however, found that SW effects can be more important in the IO than is found here. Perhaps this discrepancy is partly due to the use of canonical ISOs, rather than the observed events studied here, or partly due to the ~14% underestimation of SW fluxes by the estimated ISCCP data (Figure 3). The apparent importance of wind speed processes over wind stress processes in the BOB, and to a lesser degree in the AS, appears to be different from *Schiller and Godfrey* [2003], who suggested the importance of precipitation due to the barrier layer effect [*Lukas and Lindstrom*, 1991; *Sprintall and Tomczak*, 1992]. These aspects will be further discussed for specific ISO events below.

3.5. Specific Events and Composite MJO

[29] To reveal the spatial patterns of SST induced by ISOs in the IO, strong MJO and submonthly cooling events are identified using Figure 8. The term *strong* refers to events during which the maximum SST cooling is larger than 1 STD. Although cooling is used to choose the events, we

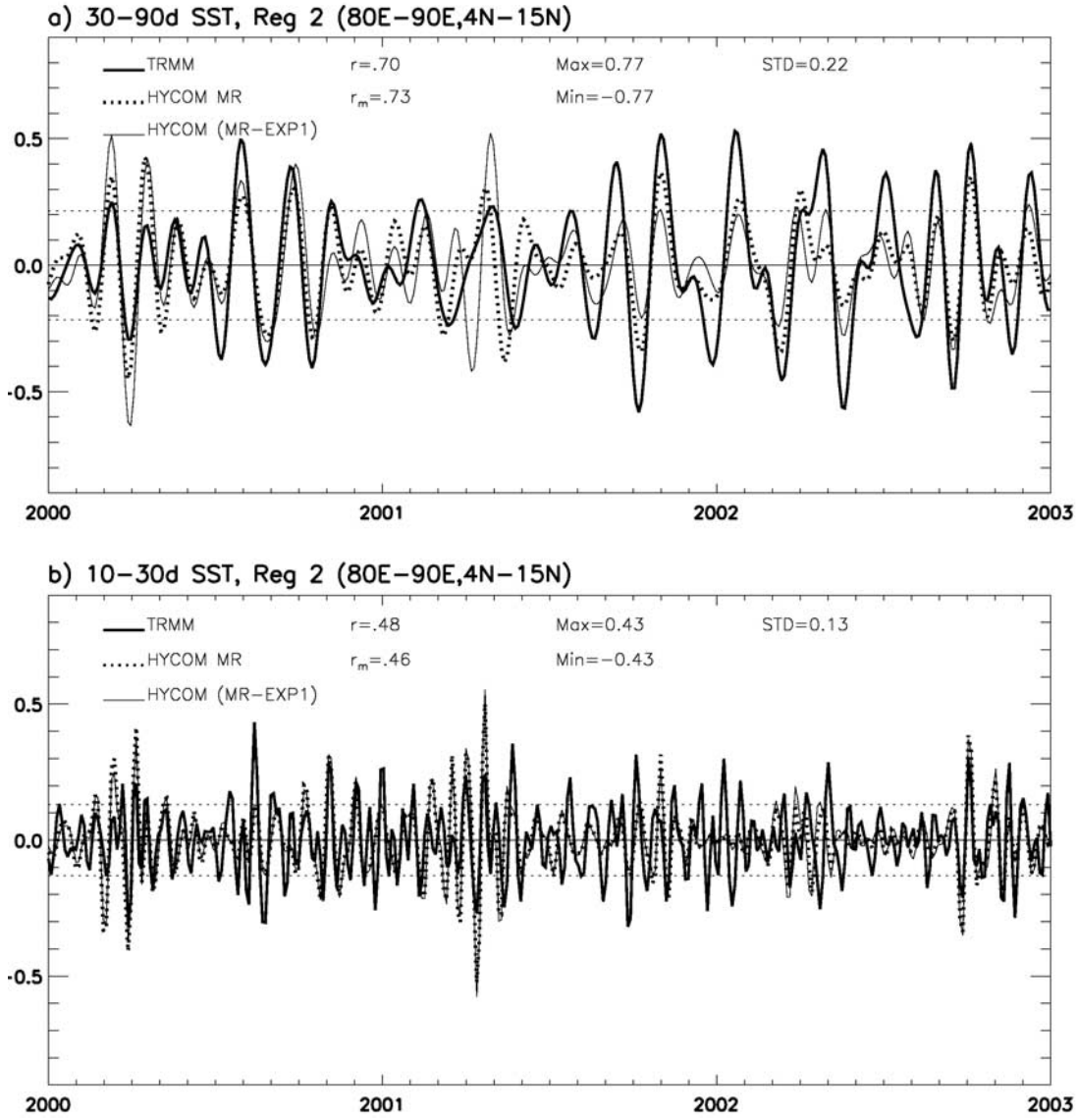

Figure 8. (a) Same as Figure 7b, except band-pass filtered to 30–90 days. (b) Same as Figure 8a, but band-pass filtered to 10–30 days.

examine the full life cycle of each. Thus, the warming phase of each chosen intraseasonal SST event is also investigated. While many cases are evaluated, we choose two representative cases for 30–90 day and submonthly SST variability and discuss the common features below.

3.5.1. A Strong MJO Event

[30] A strong MJO-scale event is identified based on the BOB time series (Figure 8a), but can also be seen in the warm pool and in the AS. The peak BOB cooling occurs on 25 August 2000, with subsequent warming on 21 September 2000 (Figure 12). HYCOM simulates the SST variations well, with warm and cold anomalies shown in similar locations and with similar magnitudes as those observed by TRMM (middle and right columns of Figure 12). For example, cool SSTs in the northern BOB and AS appear in both the TRMM data and the HYCOM solution on 3 and 12 September, with warm SSTs off the west coast of India and across the equatorial IO. TRMM SST anomalies in the BOB are typically larger than those modeled by HYCOM, an artifact that could be due to the modeled mixed layer being thicker than observed in the BOB, as investigated below.

[31] Interestingly, temporal evolution of the event shows that strong convection (negative OLR anomaly, left column of Figure 12) and its associated winds, together with cool SSTs, appear to move northward from the equator to the Indian and Asian subcontinents during 7–25 August. Before cooling arrives in the BOB (7 August), wind anomalies are northeasterlies in the BOB and AS, westerlies in the equatorial region, and northwesterlies in the south AS. As the event develops (16 August), anomalous winds become southwesterlies in both the BOB and AS. On 25 August, the peak cooling day, winds are strong southwesterlies in the northern hemisphere and easterlies along the equator. After the cooling event has completely passed through the IO basin (21 September), winds are generally as they were on

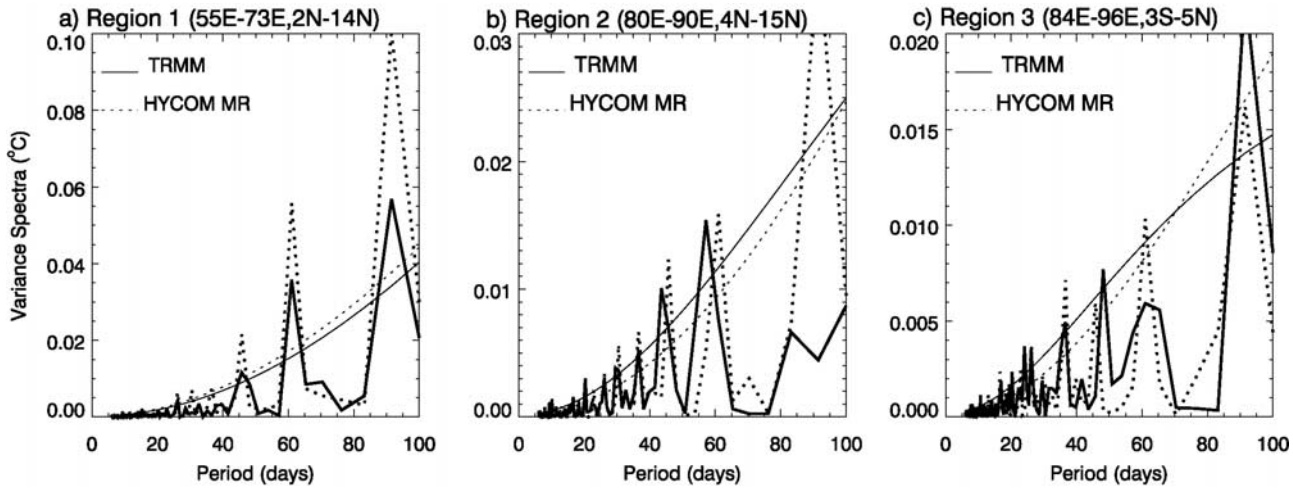

Figure 9. (a) Variance spectra of observed TRMM SST (bold line) and modeled HYCOM MR SST (bold dashed line) during summer days from 1999 to 2003, averaged over the AS (region 1). The thin solid/dashed lines show the 90% significance level for each. (b) Same as Figure 9a but for the western BOB (region 2). (c) Same as Figure 9a but for the eastern equatorial warm pool (region 3). Units are degrees Celsius.

7 August. The anomalous SST apparently lags the convection and winds. While increased convection arrives at the northern AS and BOB on 16 August, cool SST anomalies remain near the equator in the south AS and BOB. By 25 August and 3 September when strong convection moves to the northern Bay and then to the Indian subcontinent, strong negative SST anomalies first appear in the south central and then northern parts of the two basins. This delay is in agreement with *Bhat et al.* [2001] and *Webster et al.* [2002].

[32] Consistent with the general analysis in section 3.4, wind effects dominate over SW radiation and precipitation during this MJO event (Figures 13a and 13b versus Figure 13c–13d, 13i–13j, and 13k–13l), and wind speed plays a larger role than wind stress in the BOB (Figures 13c–13d versus Figures 13e–13f and 13g–13h). On both 25 August and 21 September 2000, (the event peak cooling and warming days), wind speed is the strongest forcing in the BOB. While wind stress also plays a role in causing SST anomalies there, its effect is smaller in both geographic extent and magnitude. SW radiation can be important for specific cases in specific regions, especially in the BOB, as suggested by *Han et al.* [2006a].

[33] During the peak cooling phase of this event (25 August), the anomalous southwesterly winds in the BOB and AS (Figure 12, left) enhance the mean southwest monsoon winds (Figure 5) and produce positive wind speed anomalies (Figure 13e, bold contours). The strengthened winds enhance turbulent heat fluxes and result in negative heat flux anomalies (Figure 14c), producing the surface cooling. In contrast, during the warming phase the reduced wind speed (Figures 5 and 12, and the dashed contours of Figure 13f) produces a positive heat flux anomaly (Figure 14d) and thus warms the sea surface. In the AS, the stronger (weaker) wind speed increases (decreases) entrainment cooling (see section 2.3), and thickens (thins) the mixed layer (Figures 14a and 14b), contributing to the surface cooling. In the BOB, however, entrainment cooling appears to be negligible because the hm stays almost unchanged. As a result, intraseasonal SST variability in the BOB predominately results from surface heat flux due to intraseasonal winds. This is likely because the fresher river water and strong precipitation in the BOB increase the stratification and reduce the entrainment rate there [e.g., *Han et al.*, 2001; *Howden and Murtugudde*, 2001]. This causes a thinner surface mixed layer than elsewhere in the IO (Figures 15a and 15b) and forms a barrier layer, which is present both in HYCOM MR results and in Levitus and Argo observations (Figures 15c–15f). As a result of the barrier layer, even if entrainment is occurring, it will not affect SST appreciably because the warm barrier layer water is entrained to the surface. The modeled barrier layer thickness is similar to that observed in Argo float data (Figures 15e and 15f). HYCOM's mixed layer, however, is thicker than the Levitus and Argo data in the BOB and in the AS (Figures 15a and 15b, and Figures 15e and 15f). This thicker mixed layer results in modeled SST variability in the BOB and AS that is generally smaller than in the TRMM data (Figures 7, 8, and 12).

[34] Wind stress affects the SST (Figures 13g and 13h) by anomalous upwelling due to changes in Ekman pumping velocity (w_E) and by anomalous advection. The w_E (line contours in Figures 13g and 13h) is calculated with the following equation:

$$w_E = \frac{\partial}{\partial x}\left(\frac{\tau^y}{f}\right) - \frac{\partial}{\partial y}\left(\frac{\tau^x}{f}\right),$$

where τ^x and τ^y are the zonal and meridional wind stress, and f is the Coriolis parameter. In addition to wind speed, wind stress also plays an important role in the south central AS (Figures 11a, 13g, and 13h). In the southeast AS near the Maldives Islands, the effects of wind stress dominate wind speed. The anomalously warm (cold) SSTs agree well with the negative (positive) w_E anomalies there (Figures 13g

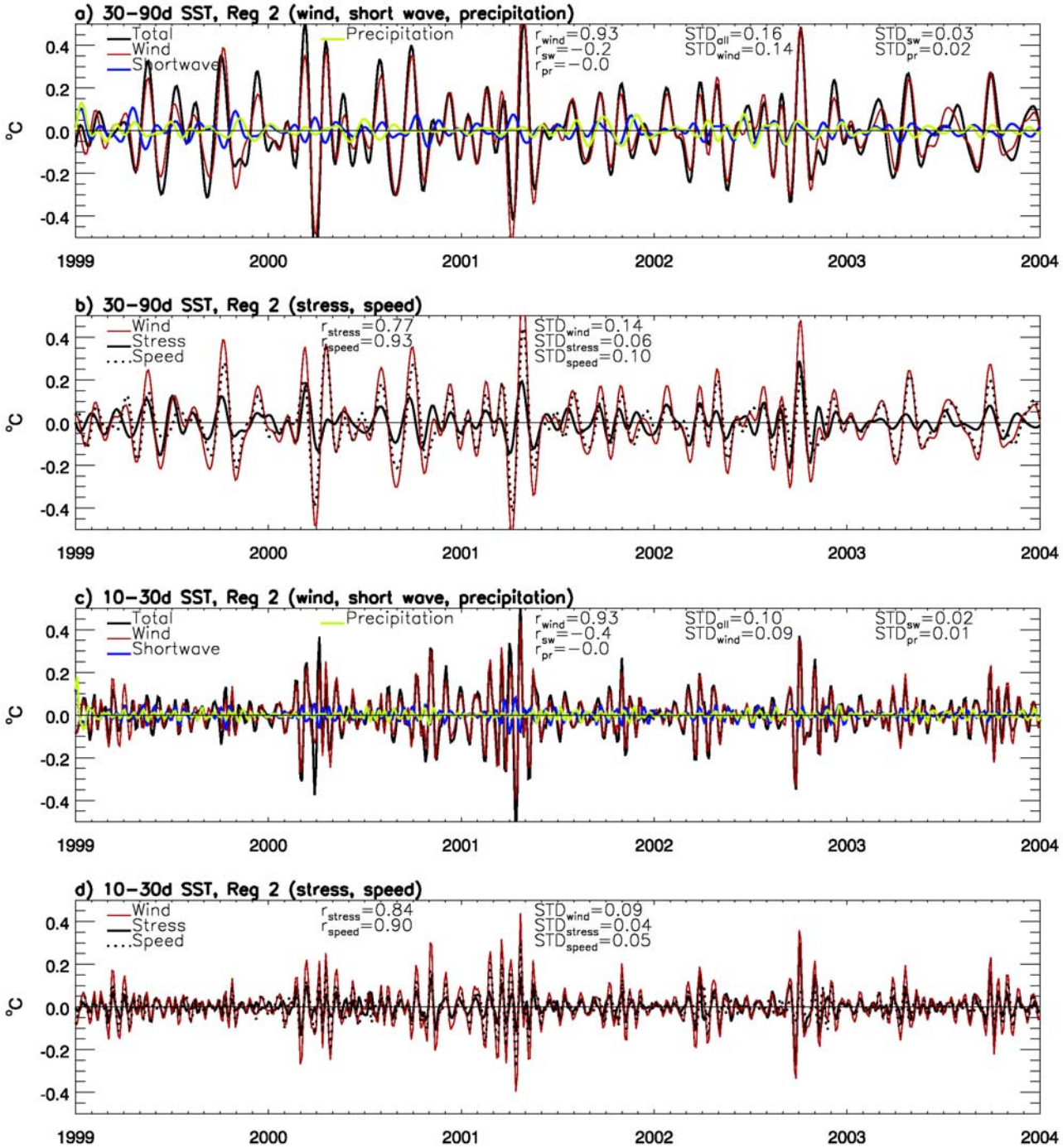

Figure 10. (a) Time series of 30–90 day SST averaged over region 2 (the BOB), forced by total ISOs (MR – EXP1, black curve), total wind (MR – EXP4, red curve), SW radiation (MR – EXP5, blue curve), and precipitation (MR – EXP6, green curve) from 1999 through 2003. (b) Same as Figure 10a but for SST caused by wind stress (MR – EXP3, solid black curve), wind speed (EXP3 – EXP4, dashed curve), and total wind (MR – EXP4, red curve). (c) Same as Figure 10a but for 10–30 day SST. (d) Same as Figure 10b but for 10–30 day SST. STDs of SST changes due to all forcings, wind speed, and stress forcings, SW radiation, and precipitation are displayed in the figures, along with the correlation coefficients (*r*) between total SST changes and those due to each process. Units are degrees Celsius.

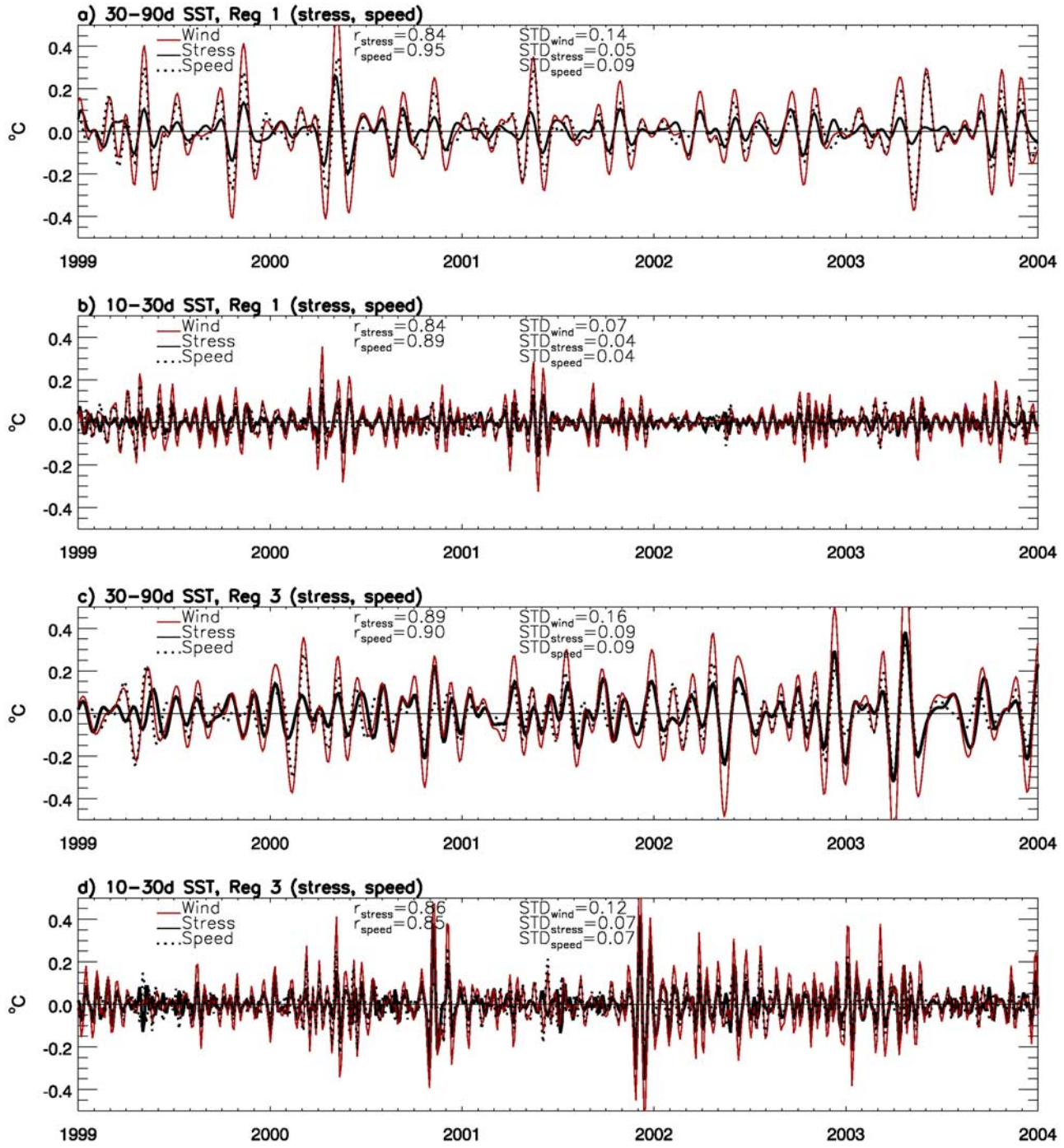

Figure 11. (a) Same as Figure 10b but for region 1 (AS). (b) Same as Figure 10d but for region 1. (c) Same as Figure 11a but for region 3 (eastern equatorial IO warm pool). (d) Same as Figure 11b but for region 3. Units are degrees Celcius.

and 13h). Anomalous horizontal advection due to wind stress is estimated using

$$\Delta T = -\left[u\frac{\partial T}{\partial x} + v\frac{\partial T}{\partial y} - \left(\overline{u}\frac{\partial \overline{T}}{\partial x} + \overline{v}\frac{\partial \overline{T}}{\partial y}\right)\right]\Delta t,$$

where u, v, and T are zonal and meridional currents and SST, respectively, from HYCOM solution MR. Terms with overbars are the same, but taken from HYCOM solution EXP3 that is forced by low-passed wind stress, and Δt is 3 days. Our results show that horizontal advection contributes little to the SST variability during this event (not shown).

[35] SST variations reach their maxima in the eastern equatorial IO warm pool on 16 August and 3 September, which leads the maximum SST variability in the BOB (Figure 12). In this region, SST variability is also controlled by winds, with wind stress and speed playing equally important roles (not shown).

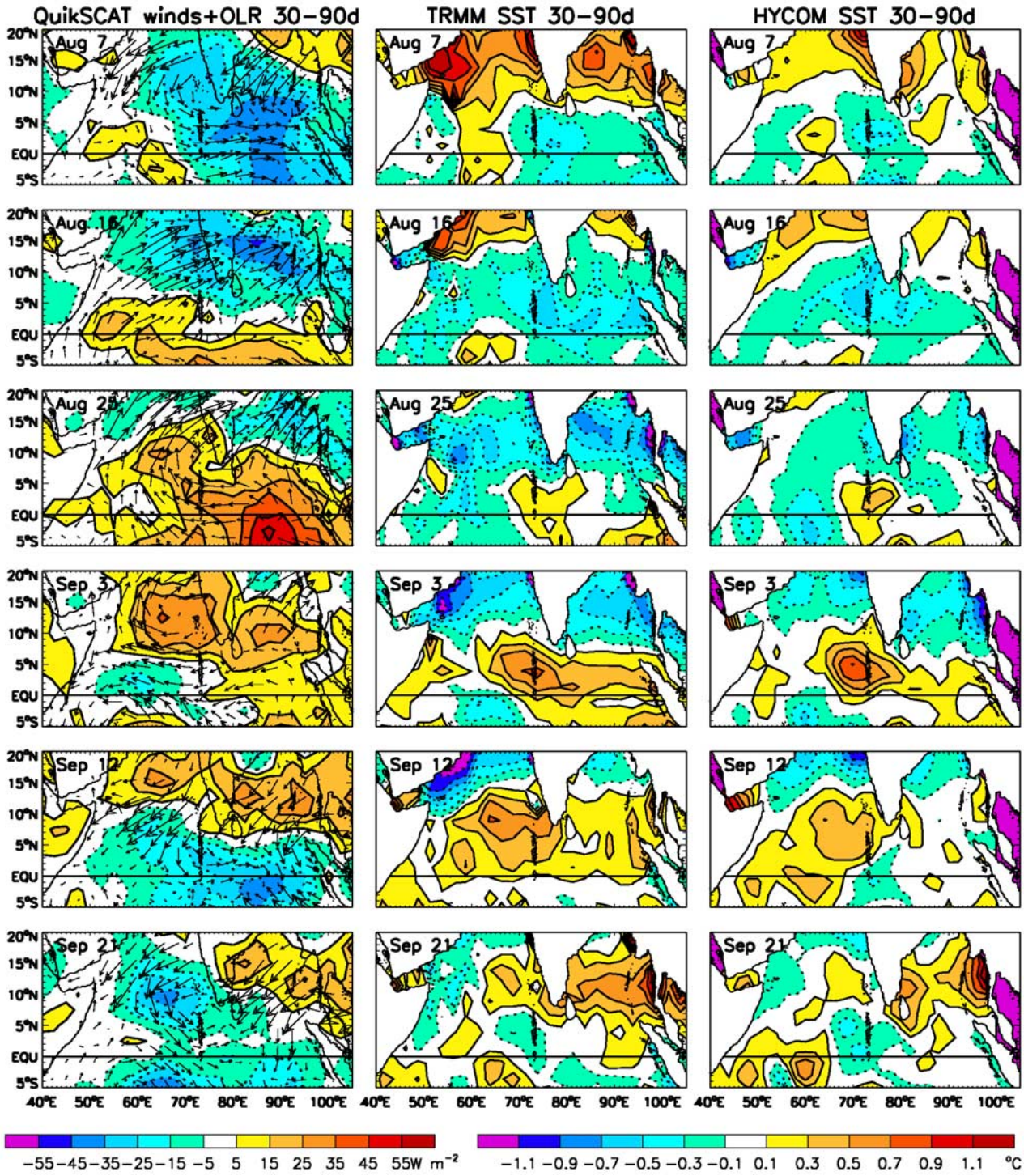

Figure 12. (left) The 30–90 day filtered QuickSCAT wind stress (arrows) and OLR (contours and shading) for a Madden-Julian Oscillation (MJO) event from 7 August to 21 September 2000 at a 9-day interval. Solid contours indicate positive values, while dashed contours indicate negative values. (middle) TRMM 30–90 day SST for the same period of time. (right) HYCOM MR 30–90 day SST for the same period of time. SST contour intervals are 0.2°C, while OLR contour intervals are 5 W m^{-2}. Units are dyn cm^{-2} for wind stress.

3.5.2. MJO Composite

[36] A composite MJO event is constructed (Figure 16), consisting of 5 separate strong summer MJO cooling events that can be seen in both TRMM and HYCOM MR SST records (Figure 8a). Each event is also associated with subsequent strong warming in both records. The peak cooling dates for the 5 events are 8 June 1999, 25 August 2000, 14 October 2000, 6 October 2001 and 15 September

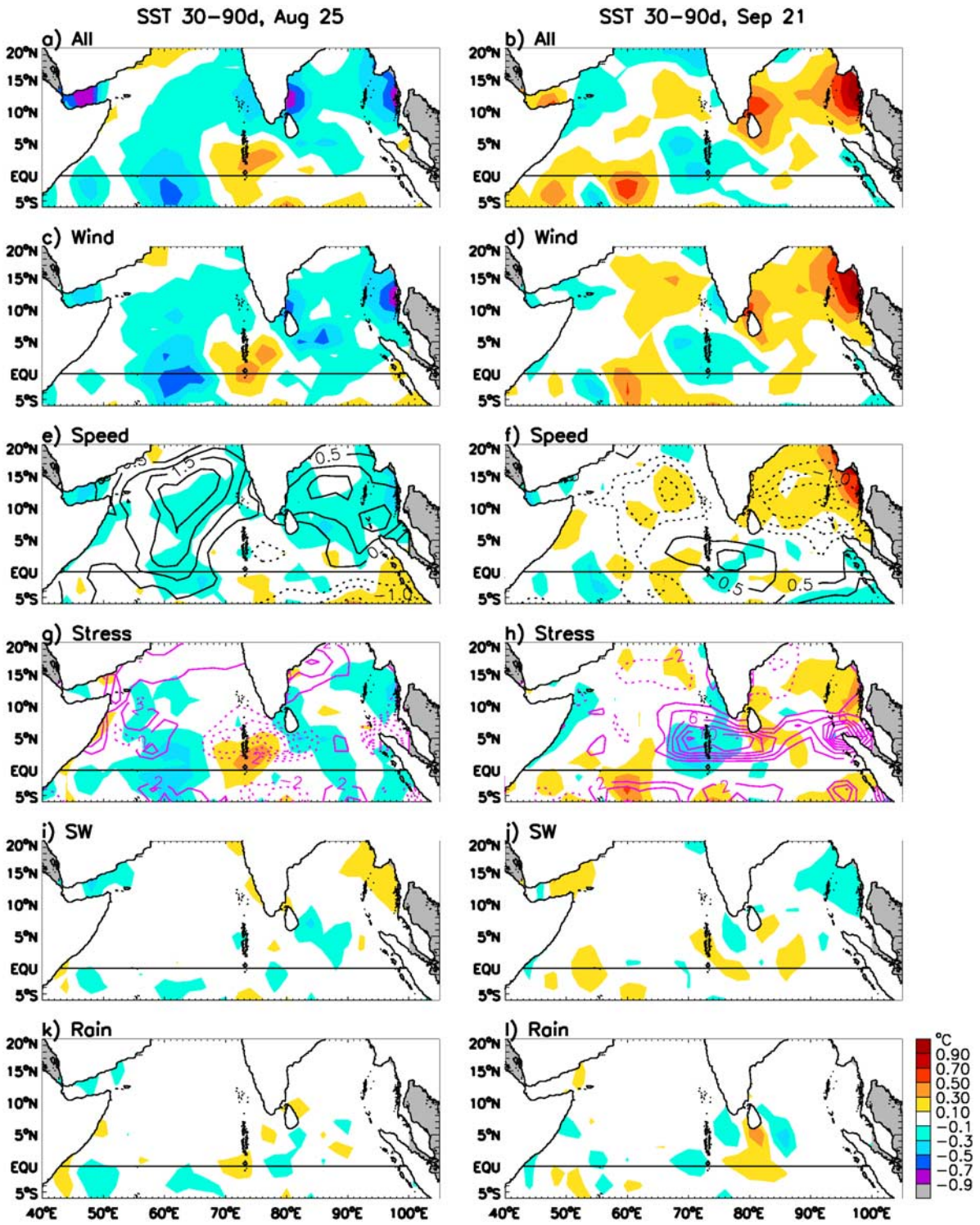

Figure 13. The 30–90 day filtered SST for (left) 25 August and (right) 21 September 2000 from a suite of HYCOM difference solutions designed to isolate processes. (a, b) SST forced by the MJO (30–90 day filtered MR – EXP1). (c, d) SST forced by the MJO wind (speed plus stress; MR – EXP4). (e, f) SST forced by the MJO wind speed only (EXP3 – EXP4). Overlying the SST is the 30–90 day wind speed (line contours) 6 days before the SST. Dashed lines show negative values (weak wind speed), and solid lines are positive values (strong wind speed). (g, h) SST forced by the MJO wind stress (MR – EXP3). Overlying the SST is the 30–90 day Ekman pumping velocity (w_E). See text for equation and definition. Positive values (upwelling) are solid, and negative values (downwelling) are dashed. (i, j) SST forced by the MJO SW radiation (MR – EXP5). (k, l) SST forced by the MJO precipitation (MR – EXP6). Units are degrees Celcius for SST, meters per second for wind speed, and 10^{-6} meters per second for w_E.

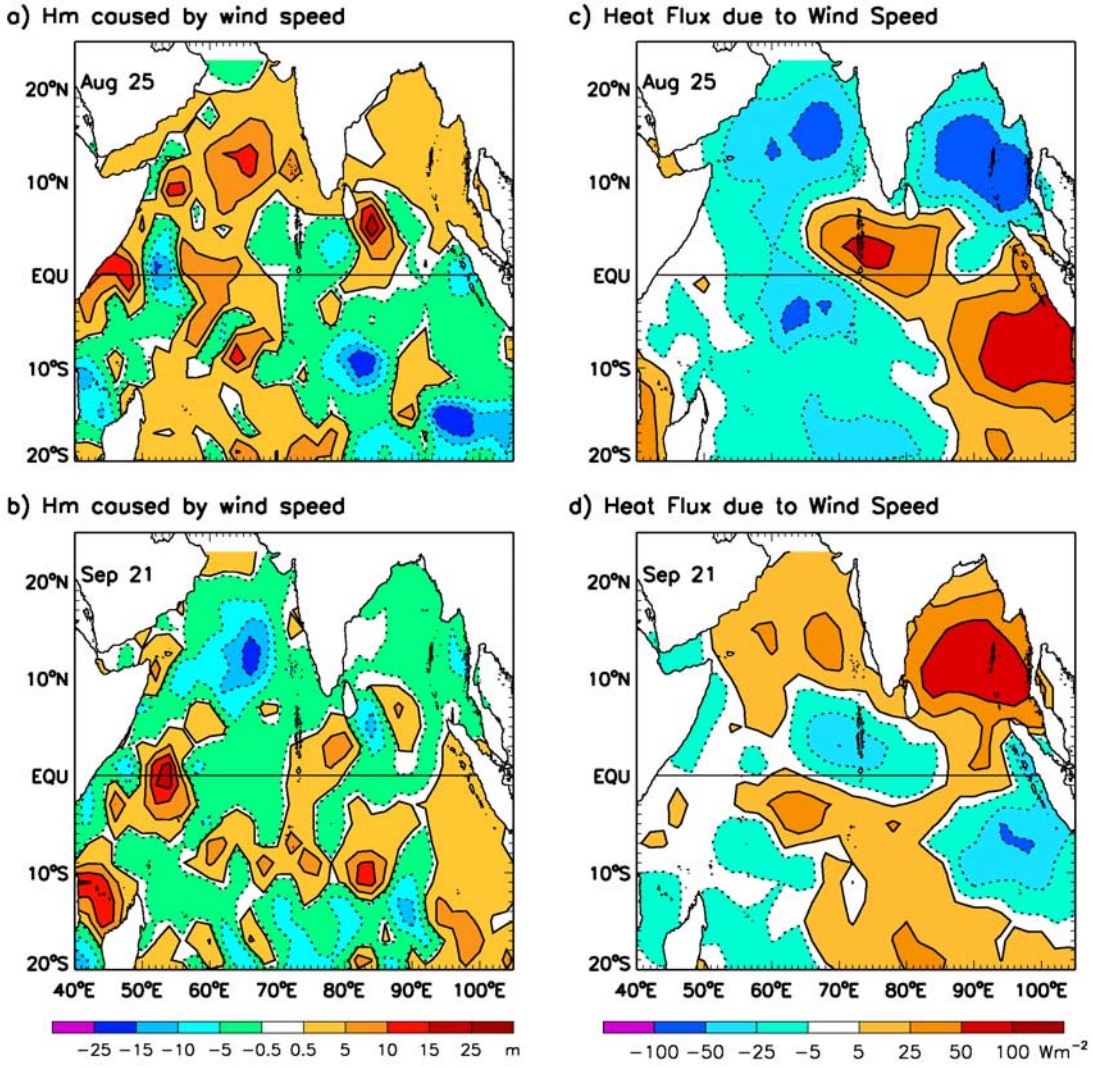

Figure 14. (a) Mixed layer thickness (hm) from HYCOM difference solution EXP3 – EXP4 (wind speed only), filtered to 30–90 days for a MJO event peak BOB cooling day (25 August 2000). Solid contours indicate positive values, while dashed contours indicate negative values. Units are in meters. (b) Same as Figure 14a but for a MJO event warming day (21 September 2000). (c) Surface turbulent heat flux during a MJO event peak cooling day, from HYCOM 30–90 day difference solution EXP3 – EXP4 (wind speed only). Units are in W m^{-2}. (d) Same as Figure 14c but for a MJO event end day.

2002. Both the OLR (Figure 16, left) and the associated SST from TRMM and HYCOM MR (middle and right columns of Figure 16) bear a remarkable resemblance to Figure 12, except that the amplitudes are weaker in the composite. This is likely because, at least partly, each MJO event has a somewhat different structure than the others, and the composite averages out some strong peaks. While the composite provides a general picture of the MJO and its impact, these results suggest that analysis of specific events is also necessary to obtain a more complete understanding of the impact of MJO events. The MJO composite TRMM and HYCOM MR SSTs in Figure 16 also show the northeastward motion associated with individual MJO events (Figure 12).

[37] Processes studies for the individual MJO events that contribute to the composite show that the relative importance of SW radiation, precipitation, and winds are consistent between the events. The conclusions from our detailed study of an MJO event, then, hold for the MJO composite.

3.5.3. A Strong Submonthly Event

[38] HYCOM does not model submonthly events as well as it models MJO events, a point highlighted by the lower 10–30 day model-data correlation coefficients in section 3.2, and further discussed below. A strong submonthly ISO cooling event overlaps with the previously discussed MJO event, occurring from 19 August to 3 September 2000, with peak cooling in the BOB on 25 August (Figure 17). HYCOM is able to capture major areas of cooling and warming in the BOB, warm pool and AS, albeit with apparent underestimations in amplitudes, particularly in the AS (middle and right columns of Figure 17). On 22 and 25 August, regions of cooling observed by TRMM in the BOB, near the warm pool, and in the eastern AS are all modeled reasonably well, with some discrepancies in mag-

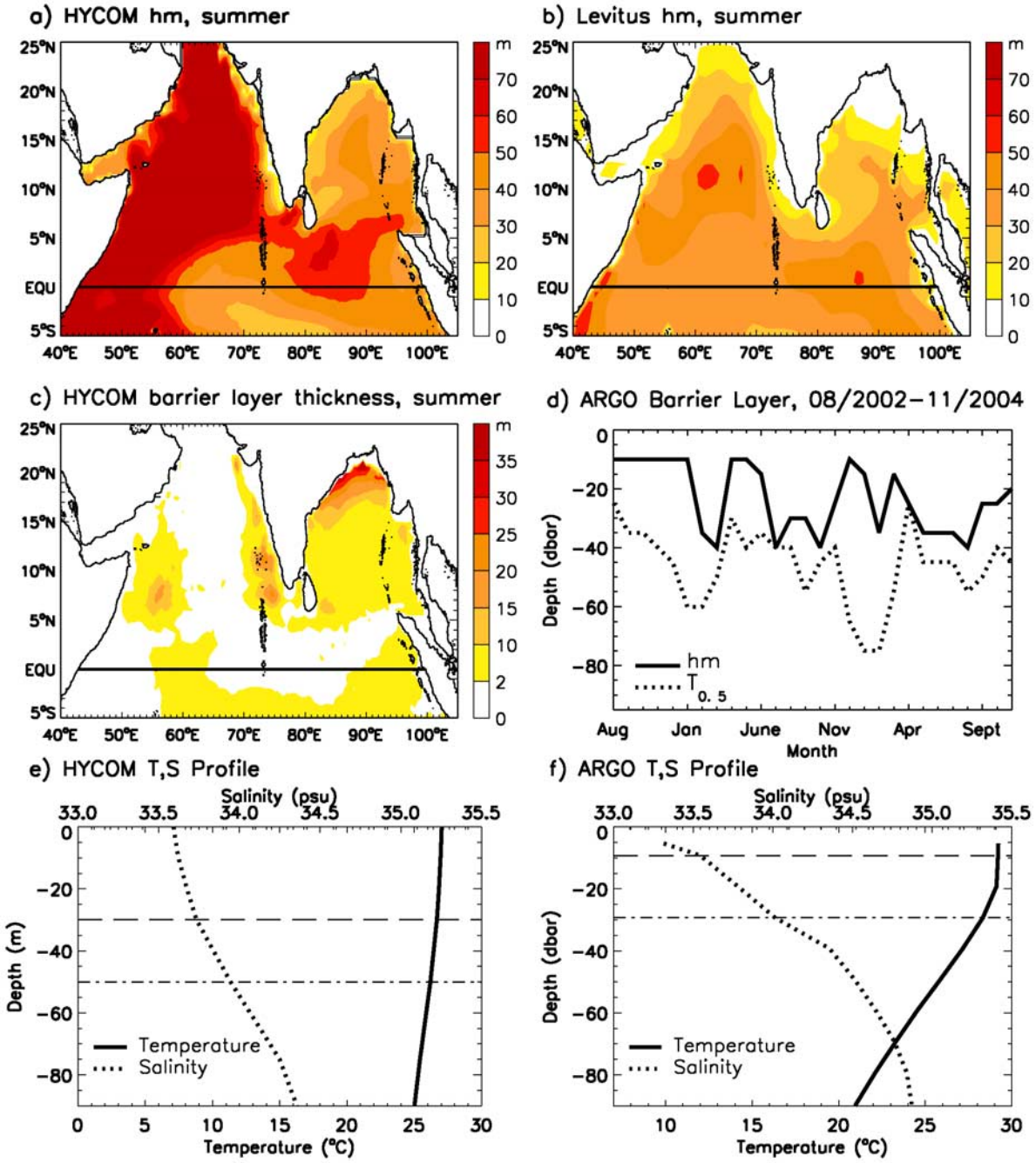

Figure 15. (a) HYCOM MR hm averaged over the summer months (May–October) from 1999 to 2003. (b) Same as Figure 15a but for Levitus data. (c) HYCOM average summertime barrier layer thickness from 1999 to 2003. Calculated using HYCOM MR mixed layer depth and the depth at which temperature decreases by 0.5°C ($T_{0.5}$). (d) Time series of Argo monthly averaged barrier layer thickness, August 2002 to November 2004, in region 2 (BOB). The difference between the hm (solid line) and $T_{0.5}$ (dotted line) is the barrier layer thickness. The hm is calculated as the depth at which the density decreases by the equivalent of 0.5°C. (e) HYCOM mean vertical temperature (solid line) and salinity (bold dotted line) profiles for a MJO event in region 2 (BOB) from 7 August to 21 September 2000. Horizontal lines indicate the calculated hm (dashed line) and $T_{0.5}$ (dash-dotted line). The distance between hm and $T_{0.5}$ is the barrier layer. (f) Same as Figure 15e, except using Argo float data. Units for all figures are in meters, except Figures 15d and 15f, which are in decibars.

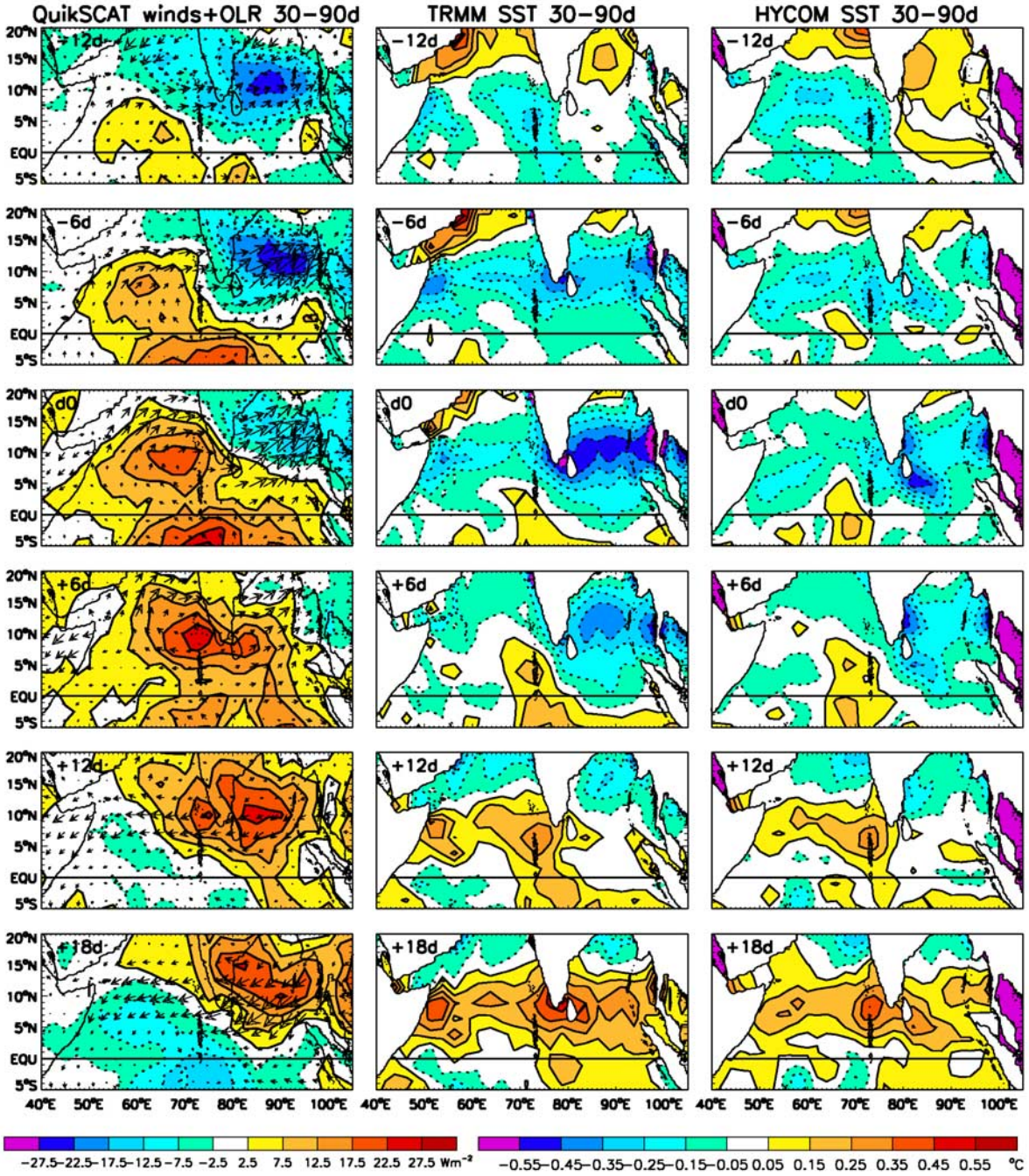

Figure 16. (left) The 30–90 day filtered QuickSCAT wind stress (arrows) and OLR (contours and shading) for a MJO composite event at a 6-day interval with respect to the date of peak BOB cooling (d_0). Solid contours indicate positive values, while dashed contours indicate negative values. (middle) TRMM 30–90 day SST for the same period of time. (right) HYCOM MR 30–90 day SST for the same period of time. SST contour intervals are 0.1°C, while OLR contour intervals are 5 W m^{-2}. Units are dyn cm^{-2} for wind stress.

nitude and geographic extent. Subsequent warming in the BOB and eastern AS is well simulated by HYCOM. As is expected from our general results, cooling is not as pronounced during this submonthly event as it is during the MJO event, even though the submonthly convection and winds are stronger. Cooler (warmer) SSTs are observed and modeled in the southeastern AS mini–warm pool region [*Rao and Sivakumar*, 1999] on 25 August (3 September). This SST variability in the mini–warm pool area (Figures 5 and 17) may have important implications for monsoon onset prediction [*Rao and Sivakumar*, 1999].

[39] Prior to the submonthly event's peak cooling in the BOB (19 and 22 August), winds in the northern AS and in the northern BOB are northeasterlies, which act to weaken

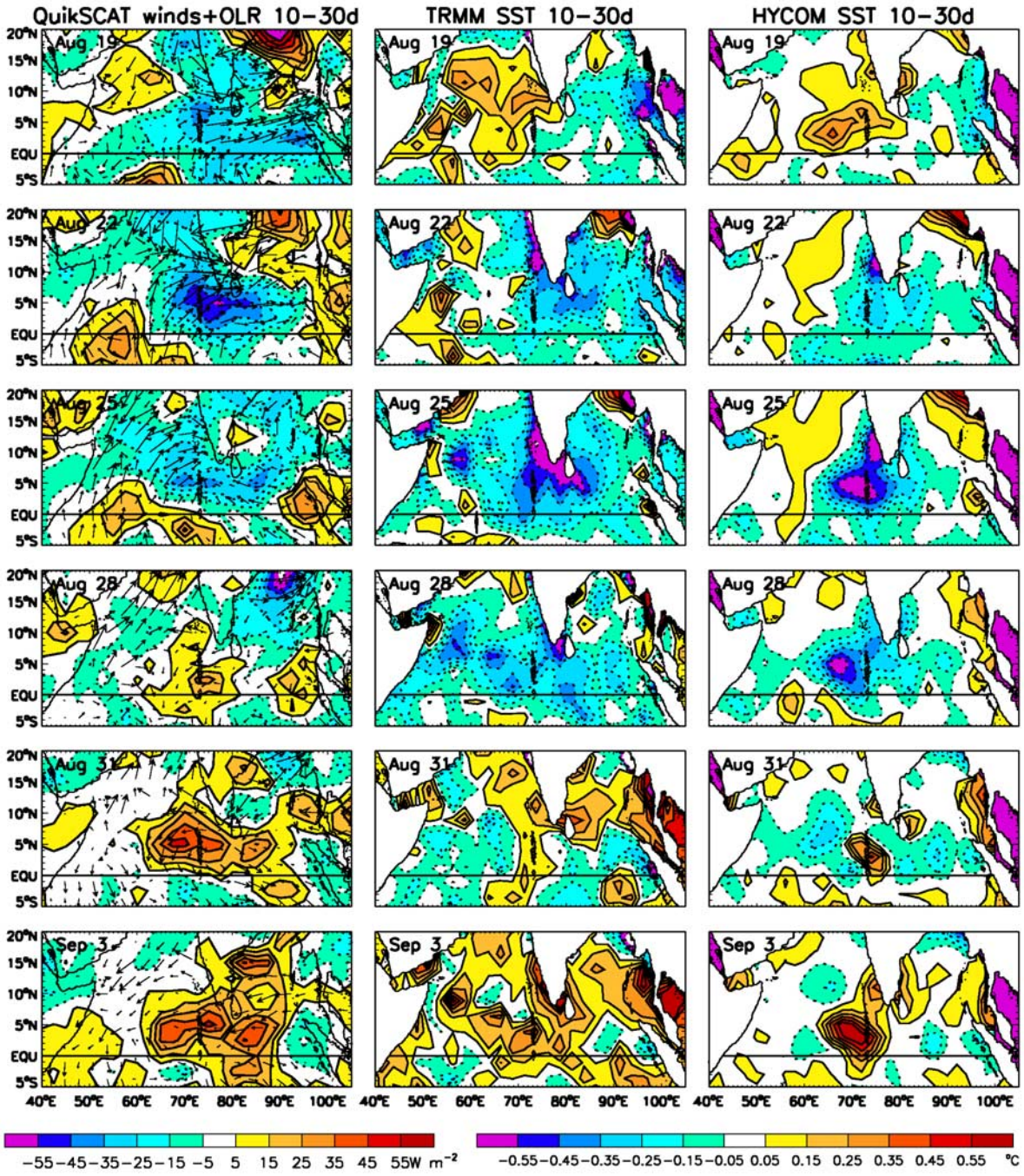

Figure 17. Same as Figure 12 but for a submonthly event from 19 August to 3 September 2000, filtered to 10–30 days and displayed at a 3-day interval with SST contour intervals of 0.1°C.

the mean summer monsoon winds (Figure 5) and thus increase SST (Figure 17, top, middle, right). Meanwhile, westerly winds prevail in the south AS, along the equator, and in the southern BOB, which enhances the mean monsoon winds and coincides with cooler SST anomalies (Figures 5 and 17). Strong convection first appears in the eastern equatorial warm pool and south of India on the 19th, and then obtains its maximum strength in the miniwarm pool region on the 22nd. On the peak cooling day of 25 August, winds in the south AS become southwesterlies, which enhances the mean monsoon and extends the cooler SST anomaly westward into the central AS. At the same time, winds in the BOB are weak with complex spatial structure. Later in the month, the anomalous southwesterlies in the AS weaken (28 August) and then reverse on the 31st, which corresponds with warmer SSTs there. Again, SST changes appear to lag the wind and convection variability (Figure 17). The spatial structures of the submonthly ISO and its associated SST show evident differences from those of the MJO. The strongest cooling produced by the submonthly ISO occurs in the mini–warm pool of the eastern AS, south of India and in the western BOB (Figure 17),

whereas the strongest cooling associated with the MJO is present across the AS and BOB (Figure 12). Wind effects again dominate SW flux and precipitation in generating the submonthly SST variability; effects of surface heat flux and entrainment cooling due to changes of wind speed are comparable to the upwelling and advection induced by variations of wind stress (figure not shown).

4. Summary and Conclusion

[40] In the present study, we use satellite observed OLR and QuickSCAT winds to document the MJO and submonthly ISOs during boreal summer. A hierarchy of experiments is performed using HYCOM (Table 1) to better understand the processes that contribute to intraseasonal SST variability. As shown in section 3, SST changes can be due to SW radiation, precipitation, surface turbulent heat fluxes and entrainment cooling associated with wind speed, and oceanic upwelling and advection associated with wind stress.

[41] While peak summer ISO forcing is the strongest on submonthly time scales (Figure 4), the peak ocean SST response occurs on MJO time scales (Figures 6e–6h). As discussed in section 3.3, this is likely because the time rate of change of SST is proportional to the forcing strength. Then, the total SST change due to an event is the integral of the forcing over time. The longer forcing period of MJO events causes a larger ocean response than the shorter, but stronger, submonthly forcing.

[42] To evaluate the relative importance of the different processes on SSTs, we choose three representative regions with strong convection, wind, and SST variability (Figures 4 and 6). Regions 1, 2, and 3 are located in the AS, the BOB, and the eastern IO warm pool, respectively (Figure 6c). Of the three, maximum summer ISO-induced SST variability is found in the warm pool (Figure 7), where maximum warming (cooling) is 0.83°C (1.09°C). The BOB also experiences strong ISO-induced SST changes, with maximum warming (cooling) of 0.78°C (1.08°C) and an STD of 0.25°C. ISO-induced SST variability is the smallest in the AS, where the mixed layer is thicker than in the BOB and equatorial warm pool (Figures 15a and 15b). Maximum warming (cooling) there is 0.67°C (0.73°C). These SST changes may have important implications in convection because the mean summer SSTs in all three regions exceed 28–29°C (Figure 5).

[43] In general, winds have much larger effects than either SW radiation or precipitation on SST variability in the three regions of interest (Figures 10a and 10c for region 2). Surface turbulent heat fluxes and entrainment cooling associated with changes in wind speed appear to have a larger effect on MJO-scale SSTs in the BOB than oceanic upwelling and advection induced by changes in wind stress (Figures 10b and 10d). In the AS, the former are just slightly stronger than the latter (Figures 11a and 11b). The same relationships hold for submonthly ISOs, albeit to a lesser extent. The effects of wind stress and wind speed appear to be comparable in the warm pool region (Figures 11c and 11d).

[44] For a more detailed analysis, many strong events (SST changes larger than 1 STD) are identified and analyzed using a time series of MJO and submonthly scale SST changes from January 2000–January 2004 (Figure 8). Of these, one MJO-scale event, an MJO composite, and one submonthly scale event are discussed in section 3.5. While the composite event is valuable for demonstrating the general MJO-scale variability, it can average out the larger amplitude changes that are visible when looking at specific MJO events (Figures 12 and 16). HYCOM appears to model SST variability in the three regions well, although it consistently underestimates the magnitude of SST changes in the BOB and AS. This is likely because the model's mixed layer is thicker than both the Levitus and the Argo observations (Figures 15a, 15b, 15e, and 15f).

[45] Consistent with our general results, surface turbulent heat fluxes and entrainment cooling induced by changes in wind speed and oceanic upwelling and advection induced by changes in wind stress are the most important in determining SST variability during both events (Figure 13 for the MJO event). Again, on the MJO time scale, turbulent heat fluxes and entrainment cooling tend to dominate in the BOB, with some contributions from upwelling and advection (Figures 13a–13b versus Figures 13e–13f and 13g–13h). Turbulent heat flux effects appear to be larger than the effects of entrainment there, as indicated by very strong heat fluxes that coincide with comparatively small changes in hm (Figure 14 for the MJO-scale event). This apparent importance of turbulent heat flux in the BOB can be attributed to a modeled and observed thin mixed layer and a barrier layer there (Figure 15). The thin mixed layer is a result of strong stratification that in turn reduces entrainment cooling. In addition, the barrier layer inhibits surface cooling due to entrainment, leaving turbulent heat fluxes as the dominant process controlling summertime SST variability in the region. Also consistent with the general results, entrainment and turbulent heat fluxes, together with upwelling, are important in causing SST variability in the AS during the two events. SW radiation appears to play a nonnegligible role in SST variability, particularly in the BOB during the MJO-scale event (Figures 13i and 13j).

[46] The SST structure and temporal evolution varies between the MJO and submonthly events. As in the general results, SST changes are stronger during the MJO event than they are during the submonthly event. The strongest submonthly SST variability is in the mini–warm pool of the eastern AS, south of India, and in the western BOB (Figure 17), while it stretches across the AS and BOB during the MJO event (Figure 12). Winds consistently enhance the prevailing summer monsoon southwesterlies in the AS and BOB during peak cooling, while they oppose it during the warming phase of the events.

[47] Overall, the effects of winds dominate IO SST variability during boreal summer ISOs, with some minor contributions from SW radiation and precipitation near the equator and in the BOB (Figures 10 and 11). Our work suggests that, in addition to surface heat fluxes, oceanic processes (upwelling and entrainment) are important in determining intraseasonal SST variability in the IO during boreal summer, particularly in the AS and warm pool region. The deterministic role of winds on SST anomalies (Figures 10, 11, and 13), and the lag between OLR and SST variability (Figure 12), may indicate that SST variations in the north IO during summer are important in modifying MJO convection, and that the MJO causes SST anomalies with its strong winds. It is hoped that this study will contribute to the understanding of coupled air-sea processes.

[48] **Acknowledgments.** We thank ECMWF and NCAR for the ERA-40 fields, the NOAA-CIRES Climate Diagnostics Center for the CMAP precipitation, Yuanchong Zhang for the ISCCP flux data, and W. Timothy Liu for preparing the QuickSCAT wind fields. The Argo data were collected and made freely available by the International Argo Project and the national programs that contribute to it (http://www.argo.ucsd.edu; http://argo.jcommops.org). Argo is a pilot program of the Global Ocean Observing System. We acknowledge NODC for making the WOA05 data available through the Internet. Thanks also go to W. G. Large, Lakshmi Kantha, Ralph Milliff, and Baylor Fox-Kemper for their valuable input. The authors are supported by NSF OCE-0452917 and NASA Ocean Vector Wind Science Team award 1283568.

References

Bajuk, L. J., and C. B. Levoy (1998), Seasonal and interannual variations in stratiform and convective clouds over the tropical Pacific and Indian Oceans from ship observations, *J. Clim.*, *11*, 2922–2941, doi:10.1175/1520-0442(1998)011<2922:SAIVIS>2.0.CO;2.

Bhat, G. S., et al. (2001), BOBMEX: The Bay of Bengal Monsoon Experiment, *Bull. Am. Meteorol. Soc.*, *82*, 2217–2243, doi:10.1175/1520-0477(2001)082<2217:BTBOBM>2.3.CO;2.

Bleck, R. (2002), An oceanic general circulation model framed in hybrid isopycnic-Cartesian coordinates, *Ocean Modell.*, *4*, 55–88, doi:10.1016/S1463-5003(01)00012-9.

Chatterjee, P., and B. N. Goswami (2004), Structure, genesis and scale selection of the tropical quasi-biweekly mode, *Q. J. R. Meteorol. Soc.*, *130*, 1171–1194, doi:10.1256/qj.03.133.

Chen, T.-C., and J.-M. Chen (1993), The 10–20 day mode of the 1979 Indian monsoon: Its relation with time variation of monsoon rainfall, *Mon. Weather Rev.*, *121*, 2465–2482, doi:10.1175/1520-0493(1993)121<2465:TDMOTI>2.0.CO;2.

Del Genio, A. D., and W. Kovari (2002), Climatic properties of tropical precipitating convection under varying environmental conditions, *J. Clim.*, *15*, 2597–2615, doi:10.1175/1520-0442(2002)015<2597:CPOTPC>2.0.CO;2.

Duchon, C. E. (1979), Lanczos filtering in one and two dimensions, *J. Appl. Sci.*, *61*, 1004–1023.

Duvel, J. P., R. Roca, and J. Vialard (2004), Ocean mixed layer temperature variations induced by intraseasonal convective perturbations over the Indian Ocean, *J. Atmos. Sci.*, *61*, 1004–1023, doi:10.1175/1520-0469(2004)061<1004:OMLTVI>2.0.CO;2.

Flatau, M., P. J. Flatau, P. Phoebus, and P. P. Niller (1997), The feedback between equatorial convection and local radiative and evaporative processes: The implications for intraseasonal oscillations, *J. Atmos. Sci.*, *54*, 2373–2386, doi:10.1175/1520-0469(1997)054<2373:TFBECA>2.0.CO;2.

Fu, R., A. D. Del Genio, and W. B. Rossow (1994), Influence of ocean surface conditions on atmospheric vertical thermodynamic structure and deep convection, *J. Clim.*, *7*, 1092–1108, doi:10.1175/1520-0442(1994)007<1092:IOOSCO>2.0.CO;2.

Fu, X., B. Wang, T. Li, and J. P. McCreary (2003), Coupling between northward propagating, intraseasonal oscillations and sea-surface temperature in the Indian Ocean, *J. Atmos. Sci.*, *60*, 1733–1783, doi:10.1175/1520-0469(2003)060<1733:CBNIOA>2.0.CO;2.

Halliwell, G. R. (2004), Evaluation of vertical coordinate and vertical mixing algorithms in the Hybrid Coordinate Ocean Model (HYCOM), *Ocean Modell.*, *7*, 285–322, doi:10.1016/j.ocemod.2003.10.002.

Han, W. (2005), Origins and dynamics of the 90-day and 30–60 day variations in the equatorial Indian Ocean, *J. Phys. Oceanogr.*, *35*, 708–728, doi:10.1175/JPO2725.1.

Han, W., D. M. Lawrence, and P. J. Webster (2001), Dynamical response of equatorial Indian Ocean to intraseasonal winds: Zonal flow, *Geophys. Res. Lett.*, *28*, 4215–4218, doi:10.1029/2001GL013701.

Han, W., P. J. Webster, R. Lukas, P. Hacker, and A. Hu (2004), Impact of atmospheric intraseasonal variability in the Indian Ocean: Low-frequency rectification in equatorial surface current and transport, *J. Phys. Oceanogr.*, *34*, 1350–1372, doi:10.1175/1520-0485(2004)034<1350:IOAIVI>2.0.CO;2.

Han, W., T. Shinoda, L. Fu, and J. P. McCreary (2006a), Impact of atmospheric intraseasonal oscillations on the Indian Ocean dipole during the 1990s, *J. Phys. Oceanogr.*, *36*, 670–690, doi:10.1175/JPO2892.1.

Han, W., W. T. Liu, and J. Lin (2006b), Impact of atmospheric submonthly oscillations on sea surface temperature of the tropical Indian Ocean, *Geophys. Res. Lett.*, *33*, L03609, doi:10.1029/2005GL025082.

Han, W., D. Yuan, W. T. Liu, and D. J. Halkides (2007), Intraseasonal variability of Indian Ocean sea surface temperature during boreal winter: Madden-Julian Oscillation versus submonthly forcing and processes, *J. Geophys. Res.*, *112*, C04001, doi:10.1029/2006JC003791.

Harrison, D. E., and G. A. Vecchi (2001), January 1999 Indian Ocean cooling event, *Geophys. Res. Lett.*, *28*, 3717–3720, doi:10.1029/2001GL013506.

Hendon, H. H., and J. Glick (1997), Intraseasonal air-sea interaction in the tropical Indian and Pacific Oceans, *J. Clim.*, *10*, 647–661, doi:10.1175/1520-0442(1997)010<0647:IASIIT>2.0.CO;2.

Hendon, H. H., and M. L. Salby (1996), Planetary-scale circulations forced by intraseasonal variations of observed convection, *J. Atmos. Sci.*, *53*, 1751–1758, doi:10.1175/1520-0469(1996)053<1751:PSCFBI>2.0.CO;2.

Howden, S., and R. Murtugudde (2001), Effects of river inputs into the Bay of Bengal, *J. Geophys. Res.*, *106*, 19,825–19,843, doi:10.1029/2000JC000656.

Inness, P. M., and J. M. Slingo (2003), Simulation of the Madden-Julian Oscillation in a coupled general circulation model. Part I: Comparison with observations and an atmosphere-only GCM, *J. Clim.*, *16*, 345–364, doi:10.1175/1520-0442(2003)016<0345:SOTMJO>2.0.CO;2.

Jerlov, N. G. (1976), *Marine Optics*, 231 pp., Elsevier, New York.

Jochum, M., and R. Murtugudde (2005), Internal variability of Indian Ocean SST, *J. Clim.*, *18*, 3726–3738, doi:10.1175/JCLI3488.1.

Jones, C., D. E. Waliser, and C. Gautier (1998), The influence of the Madden-Julian Oscillation on ocean surface heat fluxes and sea surface temperature, *J. Clim.*, *11*, 1057–1072, doi:10.1175/1520-0442(1998)011<1057:TIOTMJ>2.0.CO;2.

Kara, A. B., P. A. Rochford, and H. E. Hurlburt (2000), Efficient and accurate bulk parameterizations of air-sea fluxes for use in general circulation models, *J. Atmos. Sci. Tech.*, *17*, 1421–1438, doi:10.1175/1520-0426(2000)017<1421:EAABPO>2.0.CO;2.

Kemball-Cook, S., and B. Wang (2001), Equatorial waves and air-sea interaction in the boreal summer intraseasonal oscillation, *J. Clim.*, *14*, 2923–2942, doi:10.1175/1520-0442(2001)014<2923:EWAASI>2.0.CO;2.

Kessler, W. S. (2005), The oceans, in *Intraseasonal Variability in the Atmosphere-Ocean Climate System*, edited by W. K. M. Lau and D. E. Waliser, pp. 175–222, Springer, New York.

Kessler, W. S., and R. Kleeman (2000), Rectification of the Madden-Julian Oscillation into the ENSO cycle, *J. Clim.*, *13*, 3560–3575, doi:10.1175/1520-0442(2000)013<3560:ROTMJO>2.0.CO;2.

Kiladis, G. N., and K. M. Weickmann (1997), Horizontal structure and seasonality of large-scale circulations associated with submonthly tropical convection, *Mon. Weather Rev.*, *125*, 1997–2013, doi:10.1175/1520-0493(1997)125<1997:HSASOL>2.0.CO;2.

Krishnamurti, T. N., and D. Subramanyam (1982), The 30–50 day mode at 850 mb during MONEX, *J. Atmos. Sci.*, *39*, 2088–2095, doi:10.1175/1520-0469(1982)039<2088:TDMAMD>2.0.CO;2.

Krishnamurti, T. N., D. K. Oosterhof, and A. V. Mehta (1988), Air-sea interaction on the time scale of 30–50 days, *J. Atmos. Sci.*, *45*, 1304–1322, doi:10.1175/1520-0469(1988)045<1304:AIOTTS>2.0.CO;2.

Large, W. G., and P. R. Gent (1999), Validation of vertical mixing in an equatorial ocean model using large eddy simulations and observations, *J. Phys. Oceanogr.*, *29*, 449–464, doi:10.1175/1520-0485(1999)029<0449:VOVMIA>2.0.CO;2.

Large, W. G., J. C. McWilliams, and S. C. Doney (1994), Oceanic vertical mixing: A review and a model with a nonlocal boundary layer parameterization, *Rev. Geophys.*, *32*, 363–403, doi:10.1029/94RG01872.

Large, W. G., G. Danabasoglu, S. C. Doney, and J. C. McWilliams (1997), Sensitivity to surface forcing and boundary layer mixing in a global ocean model: Annual-mean climatology, *J. Phys. Oceanogr.*, *27*, 2418–2447, doi:10.1175/1520-0485(1997)027<2418:STSFAB>2.0.CO;2.

Lau, K. M., and P. H. Chan (1985), Aspects of the 40–50 day oscillation during the northern winter as inferred from outgoing long wave radiation, *Mon. Weather Rev.*, *113*, 1889–1909, doi:10.1175/1520-0493(1985)113<1889:AOTDOD>2.0.CO;2.

Lau, K. M., and D. E. Waliser (Eds.) (2005), *Intraseasonal Variability in the Atmosphere-Ocean Climate System*, Springer, New York.

Levitus, S., and T. P. Boyer (1994), *World Ocean Atlas 1994*, vol. 4, *Temperature, NOAA Atlas NESDIS 4*, 129 pp., NOAA, Silver Spring, Md.

Levitus, S., R. Burgett, and T. P. Boyer (1994), *World Ocean Atlas 1994*, vol. 3, *Salinity, NOAA Atlas NESDIS 3*, 111 pp., NOAA, Silver Spring, Md.

Li, T., and B. Wang (1994), The influence of sea surface temperature on tropical intraseasonal oscillation: A numerical study, *Mon. Weather Rev.*, *122*, 2349–2362, doi:10.1175/1520-0493(1994)122<2349:TIOSST>2.0.CO;2.

Liebmann, B., and C. A. Smith (1996), Description of a complete (interpolated), outgoing longwave radiation dataset, *Bull. Am. Meteorol. Soc.*, *77*, 1275–1277.

Lin, J. L., et al. (2006), Tropical intraseasonal variability in 14 IPCC AR4 climate models. Part I: Convective signals, *J. Clim.*, *19*, 2665–2690, doi:10.1175/JCLI3735.1.

Livezey, R. E., and W. Y. Chen (1983), Statistical field significance and its determination by Monte-Carlo techniques, *Mon. Weather Rev.*, *111*, 46–59, doi:10.1175/1520-0493(1983)111<0046:SFSAID>2.0.CO;2.

Lukas, R., and E. Lindstrom (1991), The mixed layer of the western equatorial Pacific Ocean, *J. Geophys. Res.*, *96*, 3343–3357, doi:10.1029/91JC01957.

Madden, R. A., and P. R. Julian (1971), Detection of a 40–50 day oscillation in the zonal wind of the tropical Pacific, *J. Atmos. Sci.*, *28*, 702–708, doi:10.1175/1520-0469(1971)028<0702:DOADOI>2.0.CO;2.

Madden, R. A., and P. R. Julian (1972), Description of global-scale circulation cells in the tropics with a 40–50 day period, *J. Atmos. Sci.*, *29*, 1109–1123, doi:10.1175/1520-0469(1972)029<1109:DOGSCC>2.0.CO;2.

McBride, J. (1987), The Australian summer monsoon, in *Reviews of Monsoon Meteorology*, edited by C. P. Chang and T. N. Krishnamurti, pp. 203–231, Oxford Univ. Press, New York.

McPhaden, M. J. (1982), Variability in the central equatorial Indian Ocean. Part II: Oceanic heat and turbulent energy balance, *J. Mar. Res.*, *40*, 403–419.

McPhaden, M. J. (1999), Genesis and evolution of the 1997–98 El Nino, *Science*, *283*, 950–954, doi:10.1126/science.283.5404.950.

Moore, A., and R. Kleeman (1999), Stochastic forcing of ENSO by the Intraseasonal Oscillation, *J. Clim.*, *12*, 1199–1220, doi:10.1175/1520-0442(1999)012<1199:SFOEBT>2.0.CO;2.

Murakami, T., and M. Frydrych (1974), On the preferred period of upper wind fluctuations during the summer monsoon, *J. Atmos. Sci.*, *31*, 1549–1555, doi:10.1175/1520-0469(1974)031<1549:OTPPOU>2.0.CO;2.

Murtugudde, R., J. P. McCreary, and A. J. Busalacchi (2000), Oceanic processes associated with anomalous events in the Indian Ocean with relevance to 1997–1998, *J. Geophys. Res.*, *105*, 3295–3306, doi:10.1029/1999JC900294.

Numaguti, A. (1995), Characteristics of 4- to 20-day period disturbances observed in the equatorial Pacific during the TOGA COARE IP, *J. Meteorol. Soc. Jpn.*, *73*, 353–377.

Rao, R. R., and R. Sivakumar (1999), On the possible mechanisms of the evolution of a mini-warm pool during the pre-summer monsoon season and the onset vortex in the southeastern Arabian Sea, *Q. J. R. Meteorol. Soc.*, *125*, 787–809, doi:10.1002/qj.49712555503.

Rao, S. A., and T. Yamagata (2004), Abrupt termination of Indian Ocean dipole events in response to intraseasonal disturbances, *Geophys. Res. Lett.*, *31*, L19306, doi:10.1029/2004GL020842.

Saji, N. H., B. N. Goswami, P. N. Vinayachandran, and T. Yamagata (1999), A dipole mode in the tropical Indian Ocean, *Nature*, *401*, 360–363.

Saji, N. H., S.-P. Xie, and C.-Y. Tam (2006), Satellite observations of intense intraseasonal cooling events in the tropical south IO, *Geophys. Res. Lett.*, *33*, L14704, doi:10.1029/2006GL026525.

Schiller, A., and J. S. Godfrey (2003), Indian Ocean intraseasonal variability in an ocean general circulation model, *J. Clim.*, *16*, 21–39, doi:10.1175/1520-0442(2003)016<0021:IOIVIA>2.0.CO;2.

Sengupta, D., B. N. Goswami, and R. Senan (2001), Coherent intraseasonal oscillations of ocean and atmosphere during the Asian summer monsoon, *Geophys. Res. Lett.*, *28*, 4127–4130, doi:10.1029/2001GL013587.

Shinoda, T., and H. H. Hendon (1998), Mixed layer modeling of intraseasonal variability in the tropical western Pacific and Indian oceans, *J. Clim.*, *11*, 2668–2685, doi:10.1175/1520-0442(1998)011<2668:MLMOIV>2.0.CO;2.

Shinoda, T. N., H. H. Hendon, and J. Glick (1998), Intraseasonal variability of surface fluxes and sea surface temperature in the tropical western pacific and Indian oceans, *J. Clim.*, *11*, 1685–1702, doi:10.1175/1520-0442(1998)011<1685:IVOSFA>2.0.CO;2.

Sikka, D. R., and S. Gadgil (1980), On the maximum cloud zone and the ITCZ over Indian longitudes during southwest monsoon, *Mon. Weather Rev.*, *108*, 1840–1853, doi:10.1175/1520-0493(1980)108<1840:OTMCZA>2.0.CO;2.

Slingo, J. M., et al. (1996), Intraseasonal oscillations in 15 atmospheric general circulation models: Results from an AMIP diagnostic subproject, *Clim. Dyn.*, *12*, 325–357, doi:10.1007/BF00231106.

Sperber, K. R., S. Gualdi, S. Legutke, and V. Gayler (2005), The Madden-Julian Oscillation in ECHAM4 coupled and uncoupled general circulation models, *Clim. Dyn.*, *25*, 117–140, doi:10.1007/s00382-005-0026-3.

Sprintall, J., and M. Tomczak (1992), Evidence of barrier layer in the surface layer of tropics, *J. Geophys. Res.*, *97*, 7305–7316, doi:10.1029/92JC00407.

Takayabu, Y. N., T. Iguchi, M. Kachi, A. Shibata, and H. Kanzawa (1999), Abrupt termination of the 1997–98 El Nino in response to a Madden-Julian Oscillation, *Nature*, *402*, 279–282, doi:10.1038/46254.

Tang, W., and W. T. Liu (1996), Objective interpolation of scatterometer winds, *Publ. 96-19*, 16 pp., Jet Propul. Lab., Pasadena, Calif.

Vincent, D. G., A. Fink, J. M. Schrage, and P. Speth (1998), High- and low-frequency intraseasonal variance of OLR on annual and ENSO timescales, *J. Clim.*, *11*, 968–986, doi:10.1175/1520-0442(1998)011<0968:HALFIV>2.0.CO;2.

Waliser, D. E., K. M. Lau, and J.-H. Kim (1999), The influence of coupled sea surface temperatures on the Madden-Julian Oscillation: A model perturbation experiment, *J. Atmos. Sci.*, *56*, 333–357, doi:10.1175/1520-0469(1999)056<0333:TIOCSS>2.0.CO;2.

Waliser, D. E., R. Murtugudde, and L. E. Lucas (2003), Indo-Pacific Ocean response to atmospheric intraseasonal variability: 1. Austral summer and the Madden-Julian Oscillation, *J. Geophys. Res.*, *108*(C5), 3160, doi:10.1029/2002JC001620.

Waliser, D. E., R. Murtugudde, and L. E. Lucas (2004), Indo-Pacific Ocean response to atmospheric intraseasonal variability: 2. Boreal summer and the Intraseasonal Oscillation, *J. Geophys. Res.*, *109*, C03030, doi:10.1029/2003JC002002.

Wang, B., and X. Xie (1997), A model for the boreal summer intraseasonal oscillation, *J. Atmos. Sci.*, *54*, 72–86, doi:10.1175/1520-0469(1997)054<0072:AMFTBS>2.0.CO;2.

Wang, B., and X. Xie (1998), Coupled modes of the warm pool climate system, part I: The role of air-sea interaction in maintaining Madden-Julian Oscillation, *J. Clim.*, *11*, 2116–2135.

Webster, P. J. (1983), Mechanisms of monsoon transition: Surface hydrology effects, *J. Atmos. Sci.*, *40*, 2110–2124, doi:10.1175/1520-0469(1983)040<2110:MOMLFV>2.0.CO;2.

Webster, P. J., and C. Hoyos (2004), Prediction of monsoon rainfall and river discharge on 15–30 day time scales, *Bull. Am. Meteorol. Soc.*, *85*, 1745–1765, doi:10.1175/BAMS-85-11-1745.

Webster, P. J., A. M. Moore, J. P. Loschnigg, and R. R. Leben (1999), Coupled ocean-atmosphere dynamics in the Indian Ocean during 1997–1998, *Nature*, *401*, 356–360, doi:10.1038/43848.

Webster, P. J., et al. (2002), The JASMINE pilot study, *Bull. Am. Meteorol. Soc.*, *83*, 1603–1630, doi:10.1175/BAMS-83-11-1603(2002)083<1603:TJPS>2.3.CO;2.

Wheeler, M., and G. N. Kiladis (1999), Convectively coupled equatorial waves: Analysis of clouds and temperature in the wavenumber-frequency domain, *J. Atmos. Sci.*, *56*, 374–399, doi:10.1175/1520-0469(1999)056<0374:CCEWAO>2.0.CO;2.

Woolnough, S. J., J. M. Slingo, and B. J. Hoskins (2000), The relationship between convection and sea surface temperature on intraseasonal timescales, *J. Clim.*, *13*, 2086–2104, doi:10.1175/1520-0442(2000)013<2086:TRBCAS>2.0.CO;2.

Woolnough, S. J., J. M. Slingo, and B. J. Hoskins (2001), The organization of tropical convection by intraseasonal sea surface temperature anomalies, *Q. J. R. Meteorol. Soc.*, *127*, 887–907, doi:10.1002/qj.49712757310.

Xie, P., and P. A. Arkin (1996), Analyses of global monthly precipitation using gauge observations, satellite estimates, and numerical model predictions, *J. Clim.*, *9*, 840–858, doi:10.1175/1520-0442(1996)009<0840:AOGMPU>2.0.CO;2.

Yasunari, T. (1981), Structure of an Indian summer monsoon system with around 40-day period, *J. Meteorol. Soc. Jpn.*, *59*, 336–354.

Yu, L. S., and M. M. Rienecker (2000), Indian Ocean warming of 1997–1998, *J. Geophys. Res.*, *105*, 16,923–16,939, doi:10.1029/2000JC900068.

Yuan, D. L., and W. Han (2006), Roles of equatorial waves and western boundary reflection in the seasonal circulation of the equatorial Indian Ocean, *J. Phys. Oceanogr.*, *36*, 930–944, doi:10.1175/JPO2905.1.

Zhang, Y., W. B. Rossow, A. A. Lacis, V. Oinas, and M. I. Mishchenko (2004), Calculation of radiative fluxes from the surface to top of atmosphere based on ISCCP and other global data sets: Refinements of the radiative transfer model and the input data, *J. Geophys. Res.*, *109*, D19105, doi:10.1029/2003JD004457.

B. Duncan and W. Han, Department of Atmospheric and Oceanic Sciences, University of Colorado, UCB 311, Boulder, CO 80309, USA. (benet.duncan@colorado.edu)